Supplements to "Nonparametric single-cell multiomic characterization of trio relationships between transcription factors, target genes, and cis-regulatory regions"

Yuchao Jiang[1,2,3,9,*], Yuriko Harigaya[4], Zhaojun Zhang[5], Hongpan Zhang[6,7], Chongzhi Zang[6,7,8], Nancy R Zhang[5,*]

[1] Department of Biostatistics, Gillings School of Global Public Health, University of North Carolina, Chapel Hill, NC 27599, USA.
[2] Department of Genetics, School of Medicine, University of North Carolina, Chapel Hill, NC 27599, USA.
[3] Lineberger Comprehensive Cancer Center, University of North Carolina at Chapel Hill, NC 27599, USA.
[4] Curriculum in Bioinformatics and Computational Biology, School of Medicine, University of North Carolina, Chapel Hill, NC 27599, USA.
[5] Department of Statistics, The Wharton School, University of Pennsylvania, Philadelphia, PA 19104, USA.
[6] Center for Public Health Genomics, University of Virginia, Charlottesville, VA 22908, USA.
[7] Department of Biochemistry and Molecular Genetics, University of Virginia, Charlottesville, VA 22908, USA.
[8] Department of Public Health Sciences, University of Virginia, Charlottesville, VA 22908, USA.
[9] Lead contact.

To whom correspondence should be addressed: yuchaoj@email.unc.edu, nzh@wharton.upenn.edu.

Supplementary Figures

Fig. S1. Reduced dimensions for single-cell multiomic datasets. a-c, UMAP (Becht et al., 2018) embedding of single cells for the 10x Genomics PBMC (from the 10x Genomics website), 10x Genomics mouse embryonic brain (from the 10x Genomics website), and SHARE-seq (Ma et al., 2020) mouse skin (from GSE140203). The three columns show UMAP embedding based on RNA, ATAC, and WNN (Hao et al., 2021), respectively, with colors corresponding to transferred/inferred cell types. The last column shows the UMAP embedding overlaid with cell-aggregate assignments. Related to Fig. 1.

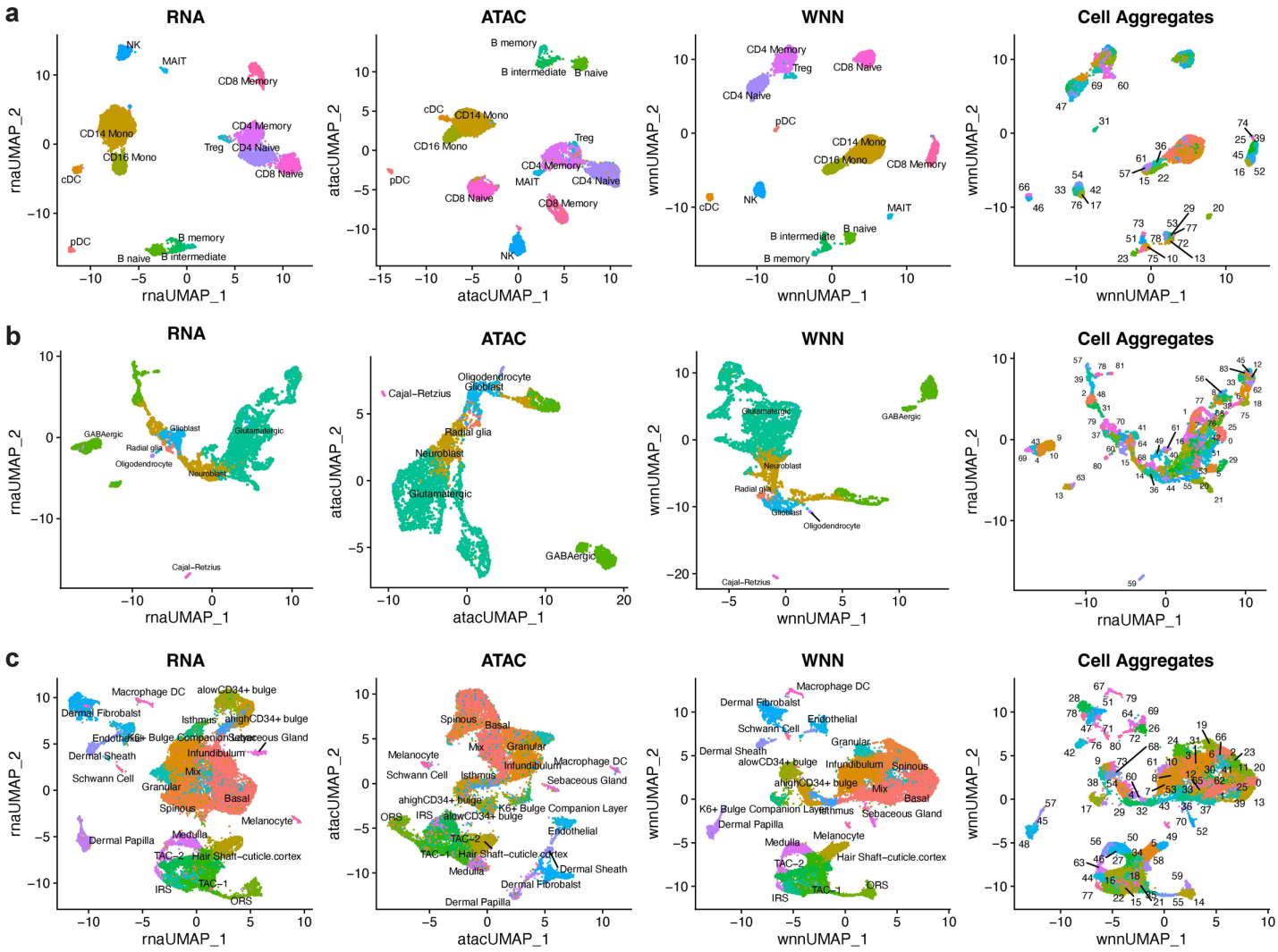

Fig. S2. Reduced dimensions and RNA prediction for SNARE-seq adult mouse brain data (Chen et al., 2019). a, UMAP embedding of single cells based on RNA, ATAC, and WNN, respectively. **b**, Box plots showing distributions of Pearson correlations between observed and out-of-fold predicted RNA expression levels across top 1000 highly variable genes. The horizontal axis represents the sizes of the windows centered at TSSs. Related to Fig. 1.

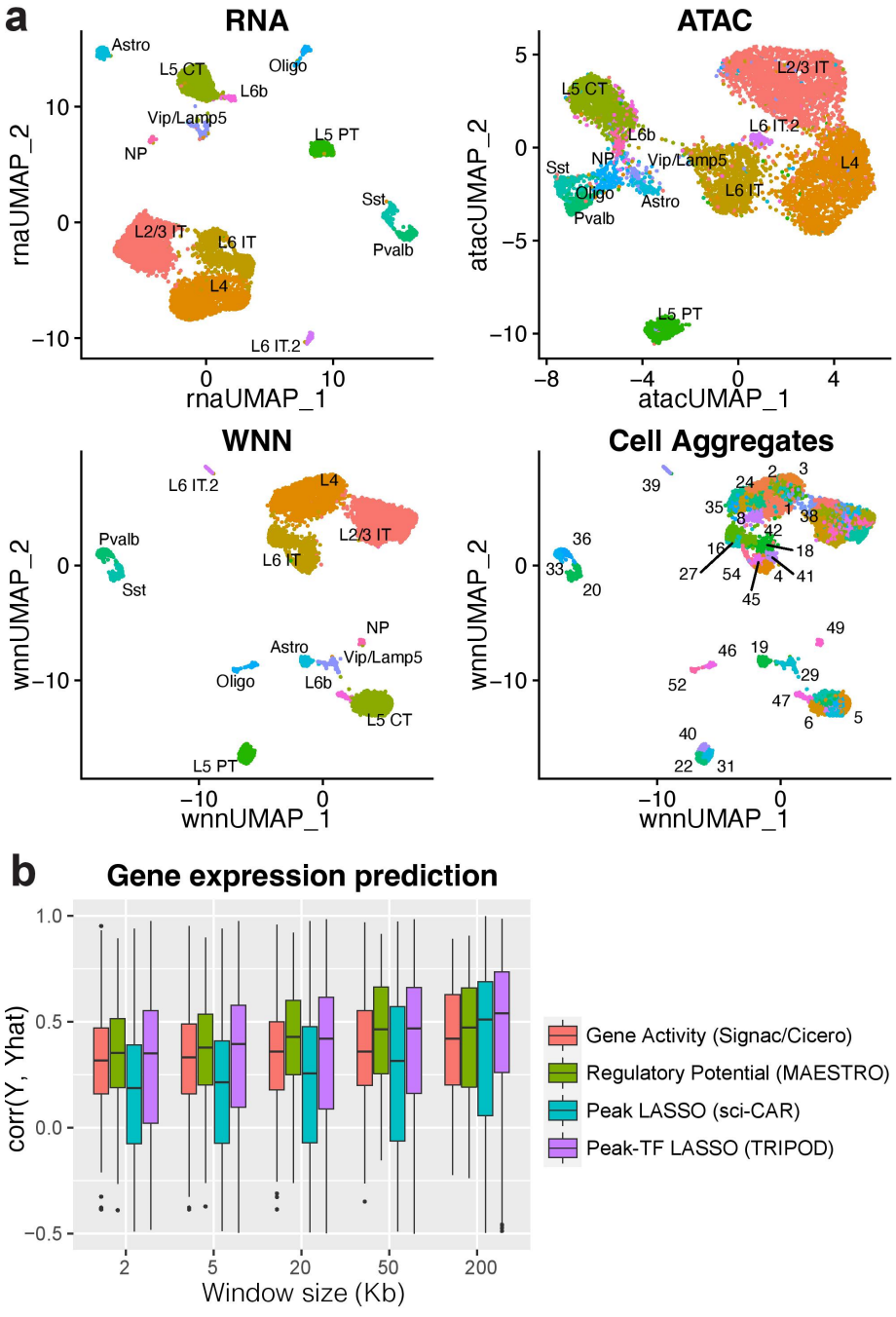

Fig. S3. RNA prediction using independent training and testing datasets of PBMC. We trained the supervised prediction model using the 10k PBMC dataset, adopted an independent single-cell multiomic dataset of 3k PBMCs as a testing dataset. We merged the two datasets to match genes, peaks, and TFs, and showed that the peak-TF LASSO model significantly increases the prediction accuracy. Distributions of Pearson correlations between observed and predicted RNA expression levels from the testing dataset are shown. Related to Fig. 1.

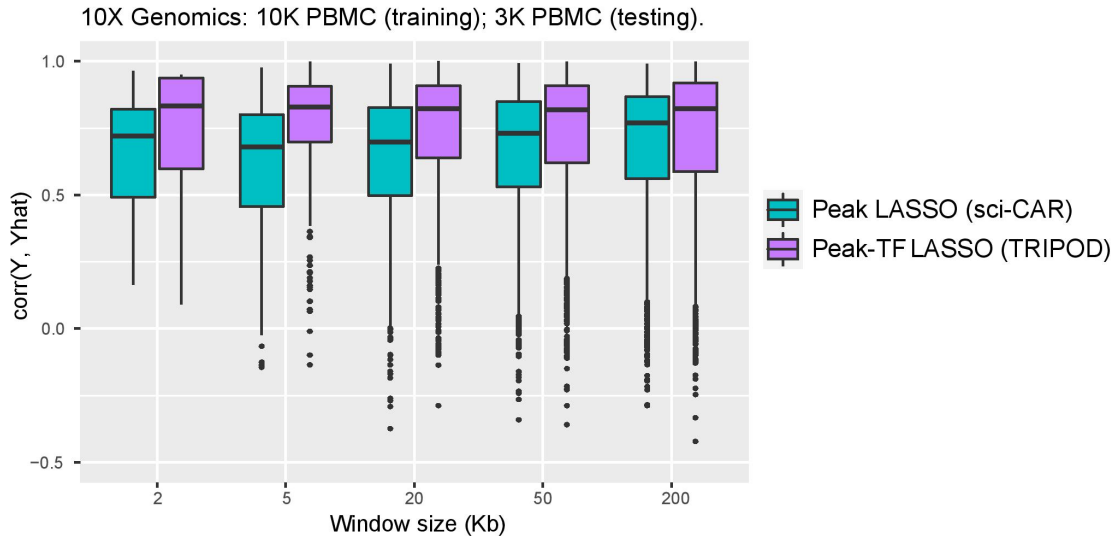

Fig. S4. RNA and ATAC coverage across different single-cell multiomic sequencing protocols. TRIPOD was applied to the 10x PBMC, 10x mouse embryonic brain, and SHARE-seq mouse skin data to detect regulatory trios. Data from SNARE-seq (Chen et al., 2019) and PAIRED-seq (Zhu et al., 2019) suffer from low sequencing depth. Related to Fig. 1.

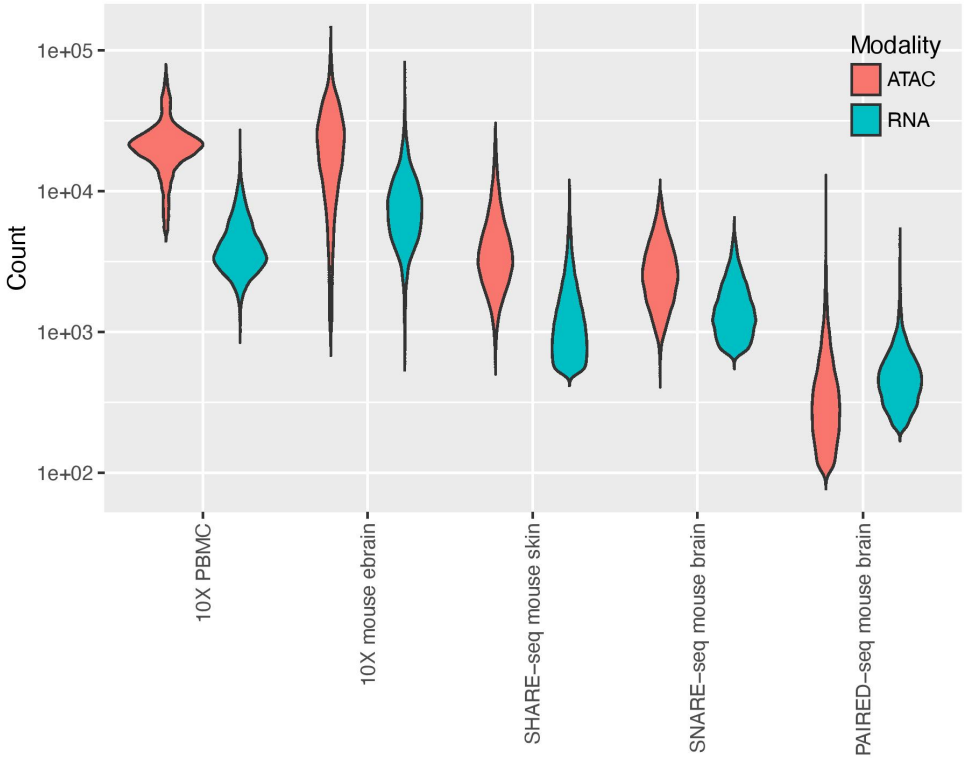

Fig. S5. Summary statistics of peaks, genes, and motifs in the PBMC data. a, Histograms of the number of peaks within regions of 100kb/200kb up and downstream of genes' TSSs. **b**, Histograms of the number of genes within regions of 100kb/200kb up and downstream of genes' TSSs. **c**, Histogram of the number of motifs per peak. Of the many possible and biologically meaningful peak-TF-gene combinations, TRIPOD proceeds to scan for trios with significant conditional associations. Related to Fig. 2.

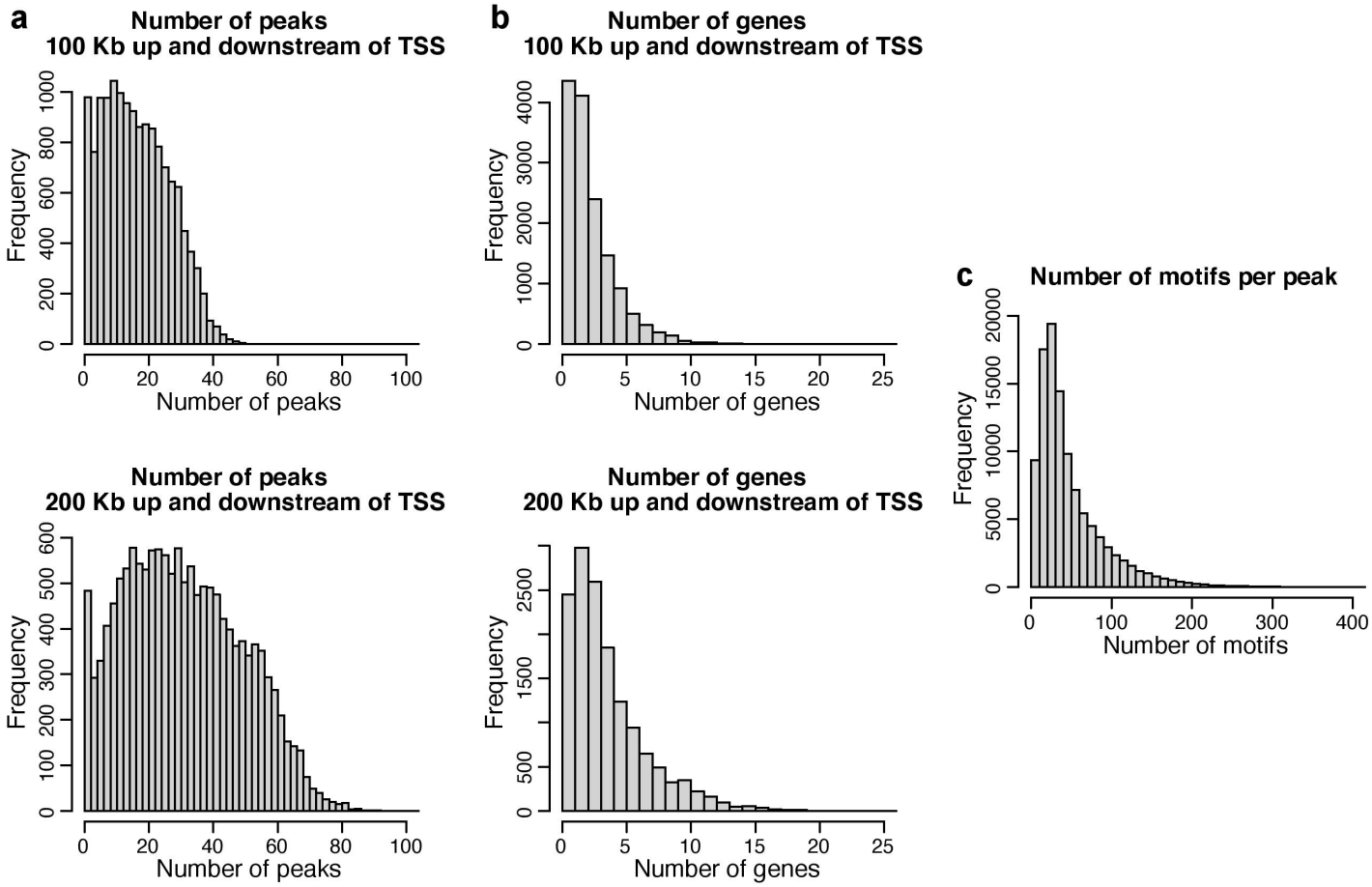

Fig. S6. Identification of putative cell-type-specific trio regulatory relationships in PBMC. Results from cell-type-specific influence analyses are shown for the same example trios as in Fig. 3. **a**, Cell-aggregate-specific Cook's distance. **b**, Cell-aggregate-specific DFFITS. **c**, Cell-type-specific influential p-values. **d**, Cell-type hierarchies constructed from the RNA domain using highly variable genes. Red/gray circles indicate whether removal of the corresponding branches of cell aggregates significantly changes the model fitting; crosses indicate that removal of the groups of cell aggregates resulted in inestimable coefficients. **e**, Cell-type-specific DNA footprinting signatures of the TF binding motifs. The enrichment results supported the key regulatory cell types identified from the influence analyses. Related to Fig. 3.

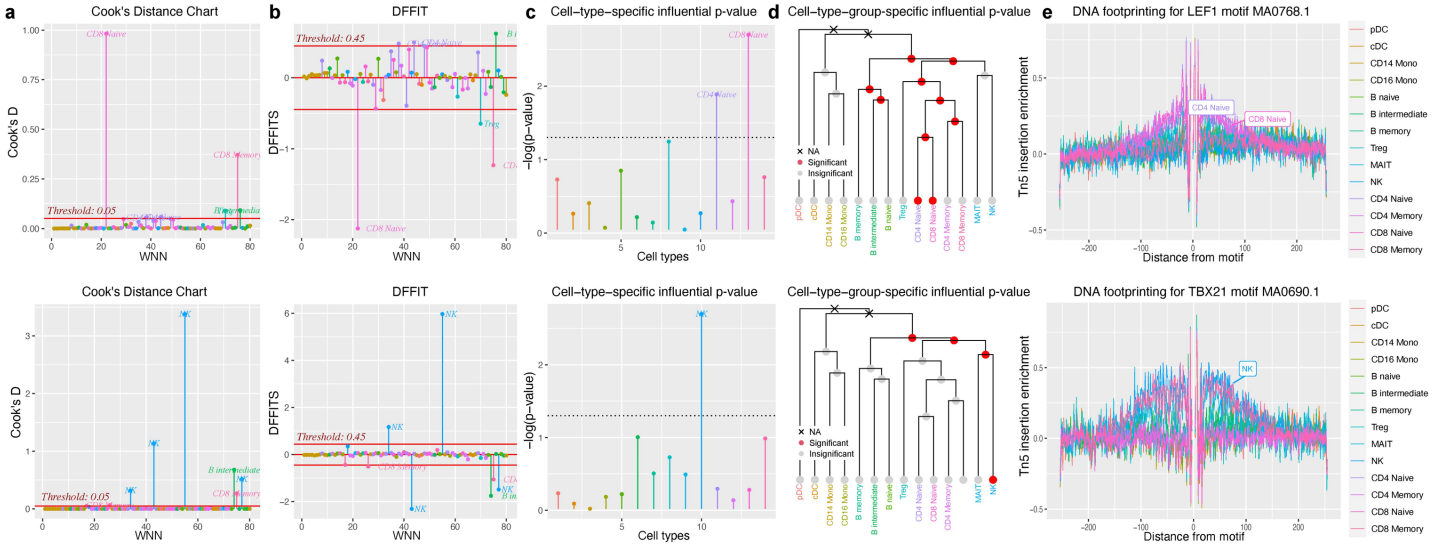

Fig. S7. Regulatory relationships identified by LinkPeaks, marginal association, and TRIPOD in the PBMC data. a, Venn diagrams of the number of peak-gene pairs captured by LinkPeaks (Stuart et al., 2021), marginal association between gene expression and peak accessibility, and TRIPOD for representative target genes (*CCR7*, *GNLY*, *FCGR3A*, and *MS4A1*). For TRIPOD, the union set between level 1 and level 2 testing matching by TF expression is shown. **b**, Venn diagrams of the number of TF-gene pairs captured by marginal association between gene expression and TF expression and TRIPOD. For TRIPOD, the union set between level 1 and level 2 testing matching by peak accessibility is shown. TRIPOD complements and contrasts with existing methods based on marginal associations. Related to Fig. 4.

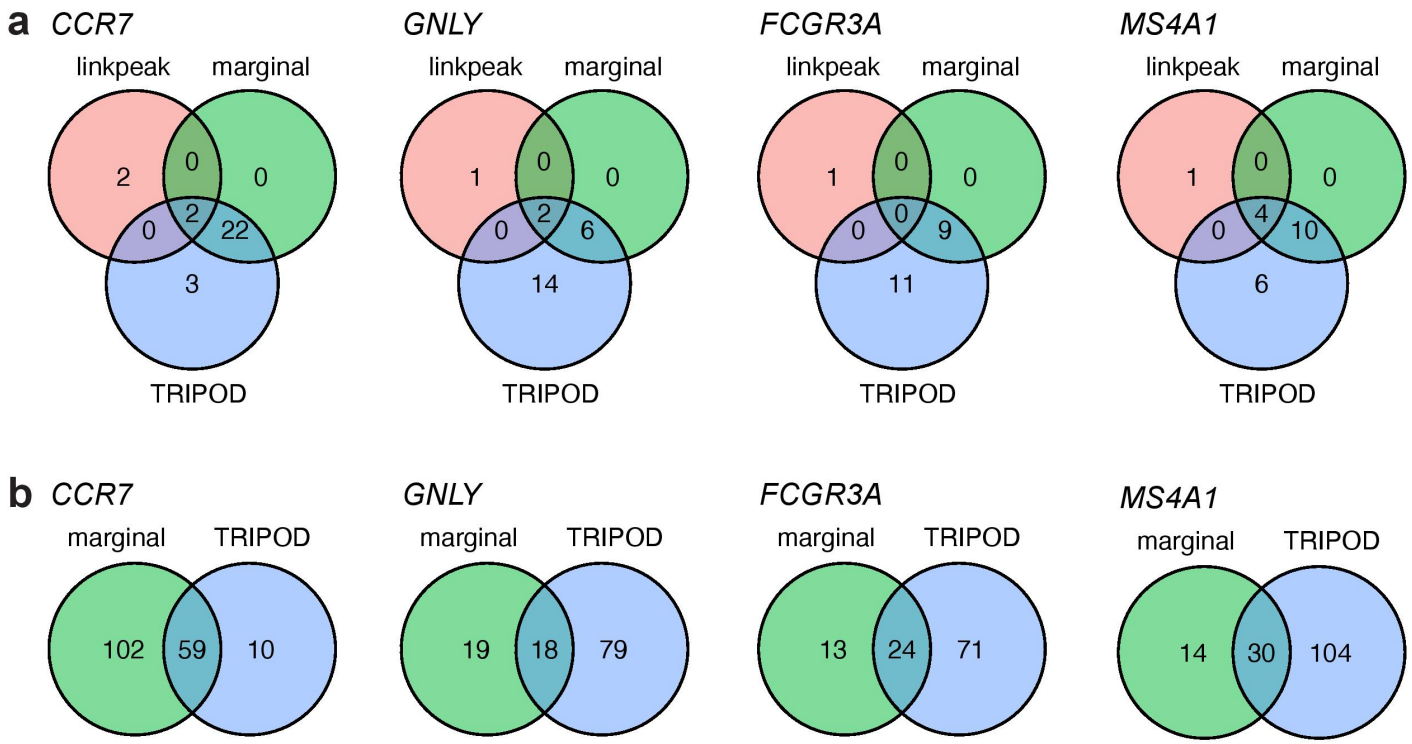

Fig. S8. Level 1 and level 2 conditional testing results from TRIPOD's matching scheme and random matching. Results from TRIPOD's matching scheme and those from random matching also overlap but exhibit substantial differences, especially for level 2 testing. Related to Fig. 4.

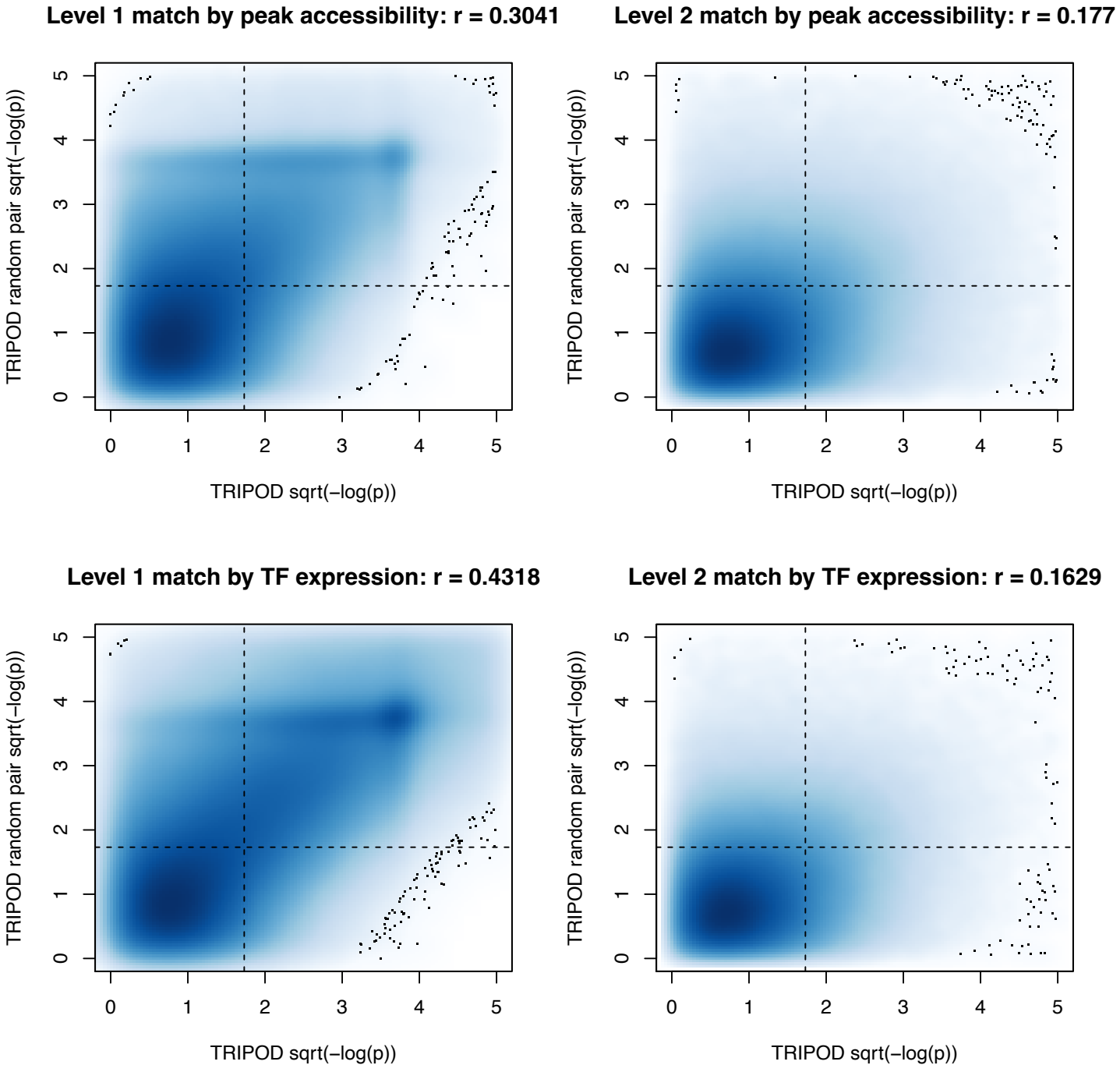

Fig. S9. Gene-specific level 1 and level 2 conditional testing results from TRIPOD's matching scheme and random matching. Results from TRIPOD's matching scheme and those from random matching also overlap but exhibit substantial differences, especially for level 2 testing. Related to Fig. 4.

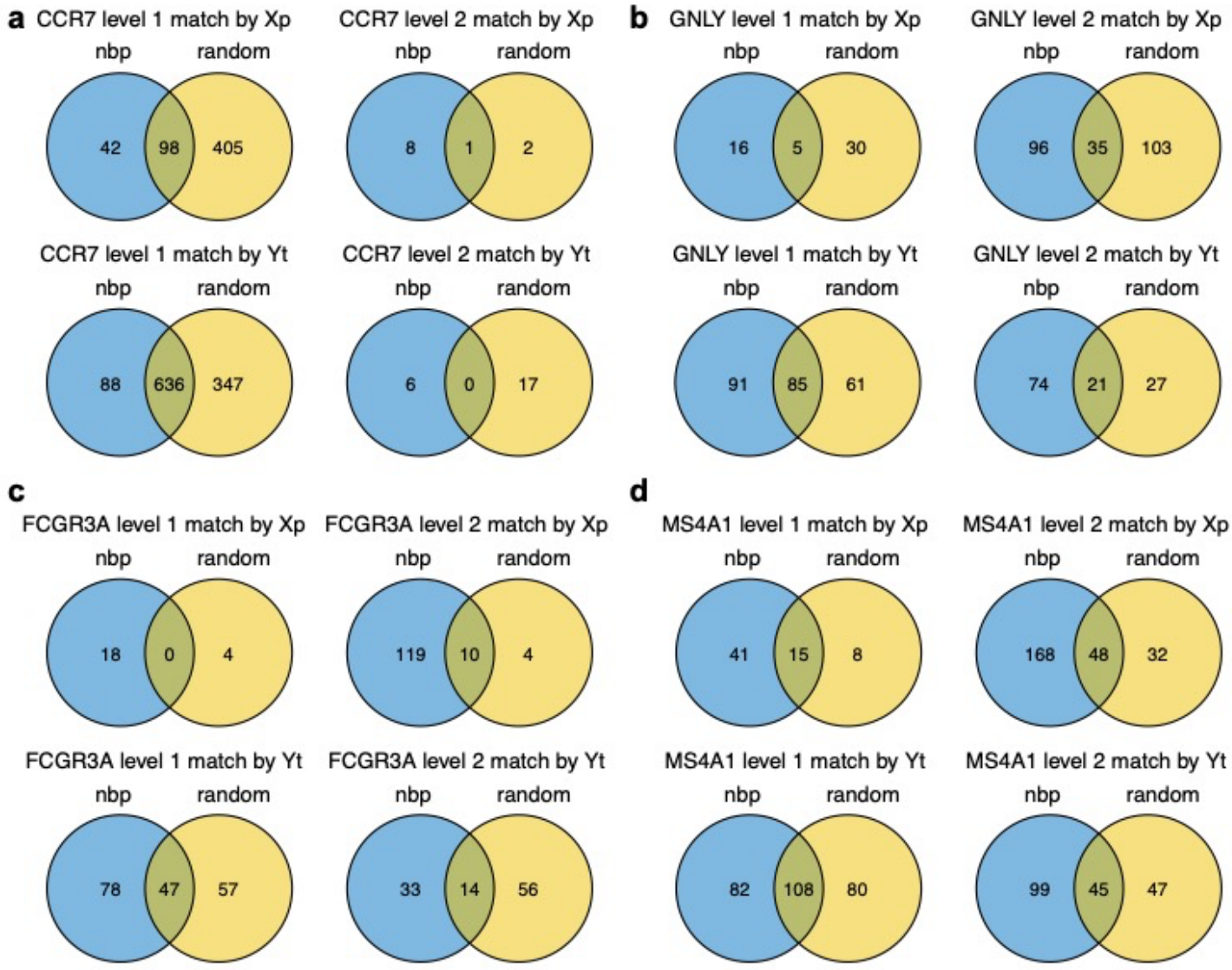

Fig. S10. Random matching suffers from false positive and false negative in the two PBMC counter examples. The same two example trios from Fig. 2 are shown with random matching, which is equivalent to marginal testing and results in (**a**) false negative and (**b**) false negative. Related to Fig. 4.

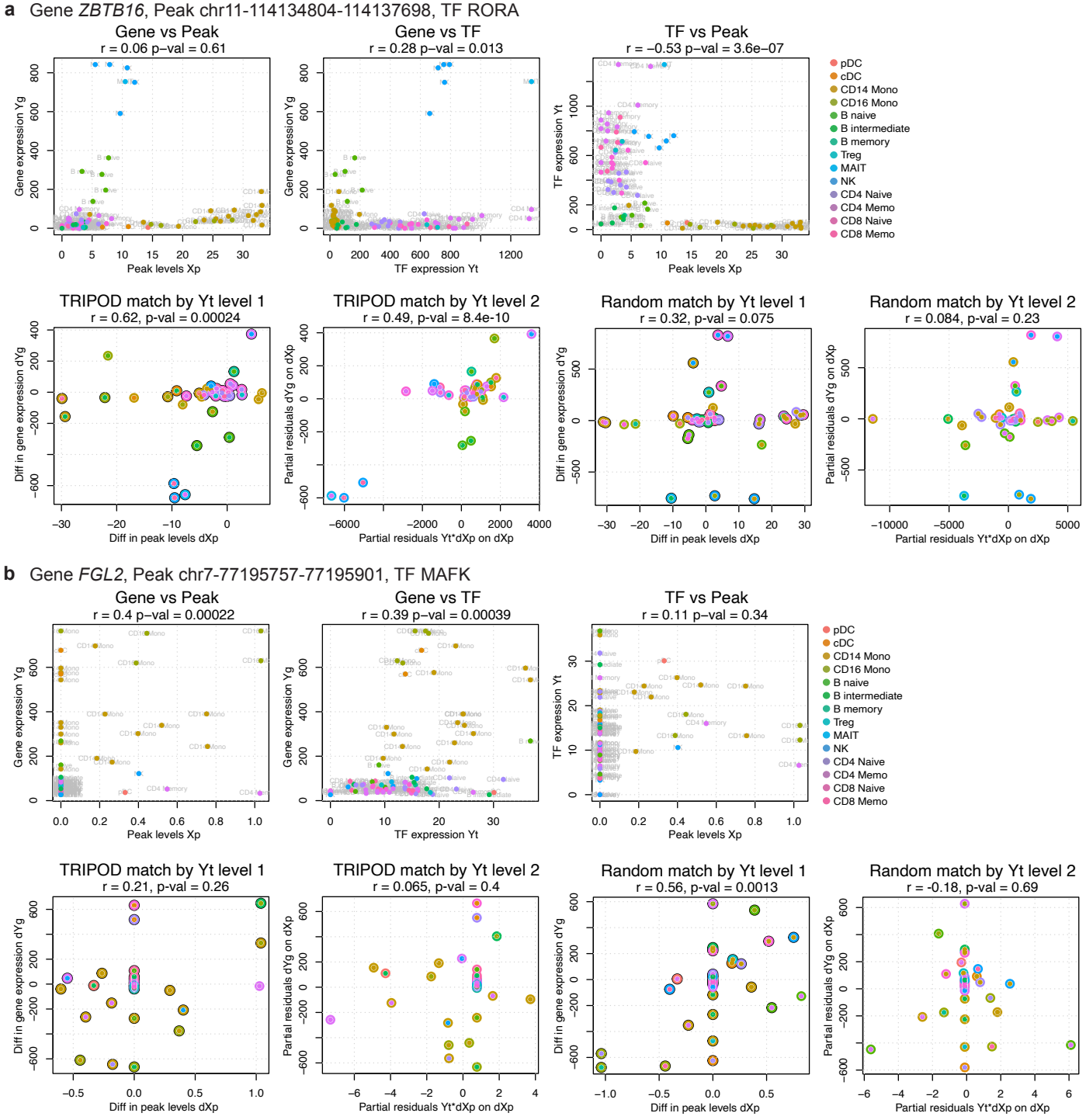

Fig. S11. TRIPOD controls for type I error via permutation-based analysis. a, TRIPOD's nominal p-value distributions on the PBMC multiomic data. **b**, Peak accessibilities and TF expressions are randomly permuted to generate trios under the null. TRIPOD's p-value distributions are uniformly distributed, indicating TRIPOD's good type I error control. Related to Fig. 4.

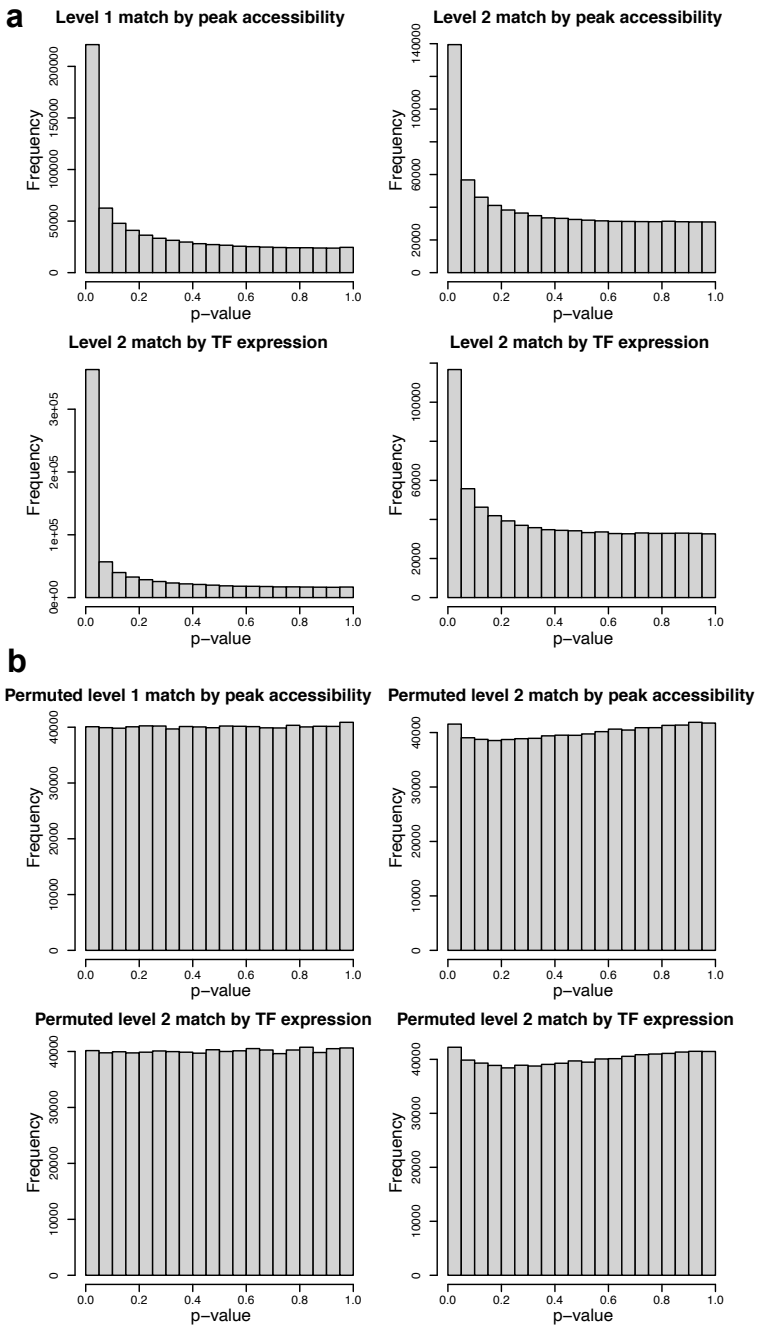

Fig. S12. Pairwise correlations of genome-wide p-values from different testing schemes. For each trio, transformed p-values – negative logarithm of p-values times the sign of the regression coefficient – from marginal association (gene~peak, gene~TF, and peak~TF), linear interaction, TRIPOD's level 1 and level 2 conditional testing matching by peak accessibility and TF expression are shown in the pairwise scatterplots with correlation coefficients shown in the upper triangle. TRIPOD's significant regulatory trios complement both existing approaches based on marginal associations and linear models. Master output is included in Data S1. Related to Fig. 4.

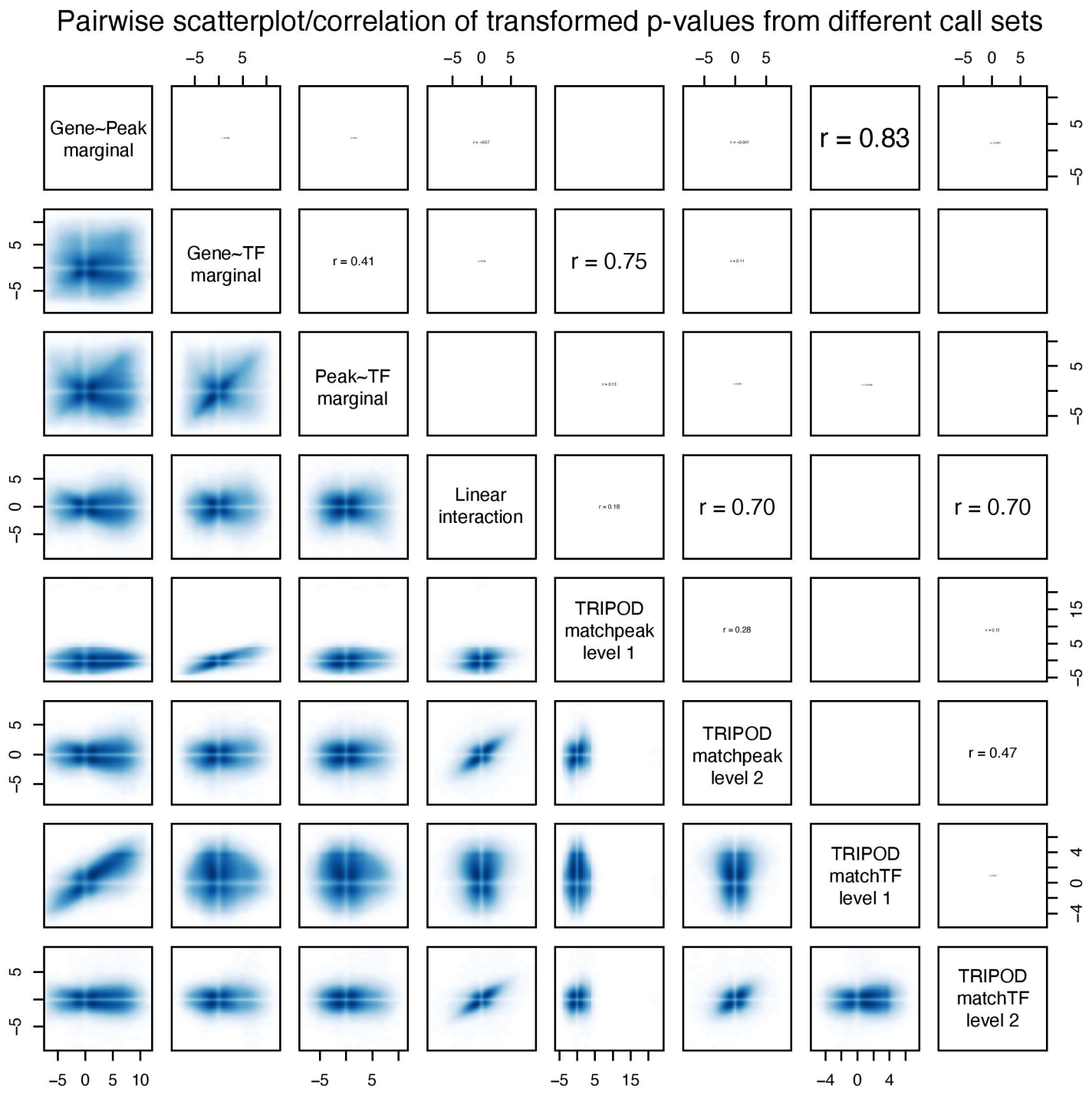

Fig. S13. TRIPOD's peak-gene validation from TRIPOD's stratified testing scheme. a, Gene-peak validation using significant trios returned by TRIPOD's level 1 and level 2 testing, matching by peak accessibility and TF expression, respectively. b, Gene-peak validation using significant trios called by TRIPOD but *not* by random matching. TRIPOD identified additional real regulatory relationships masked by methods based on marginal association testing. Related to Fig. 4.

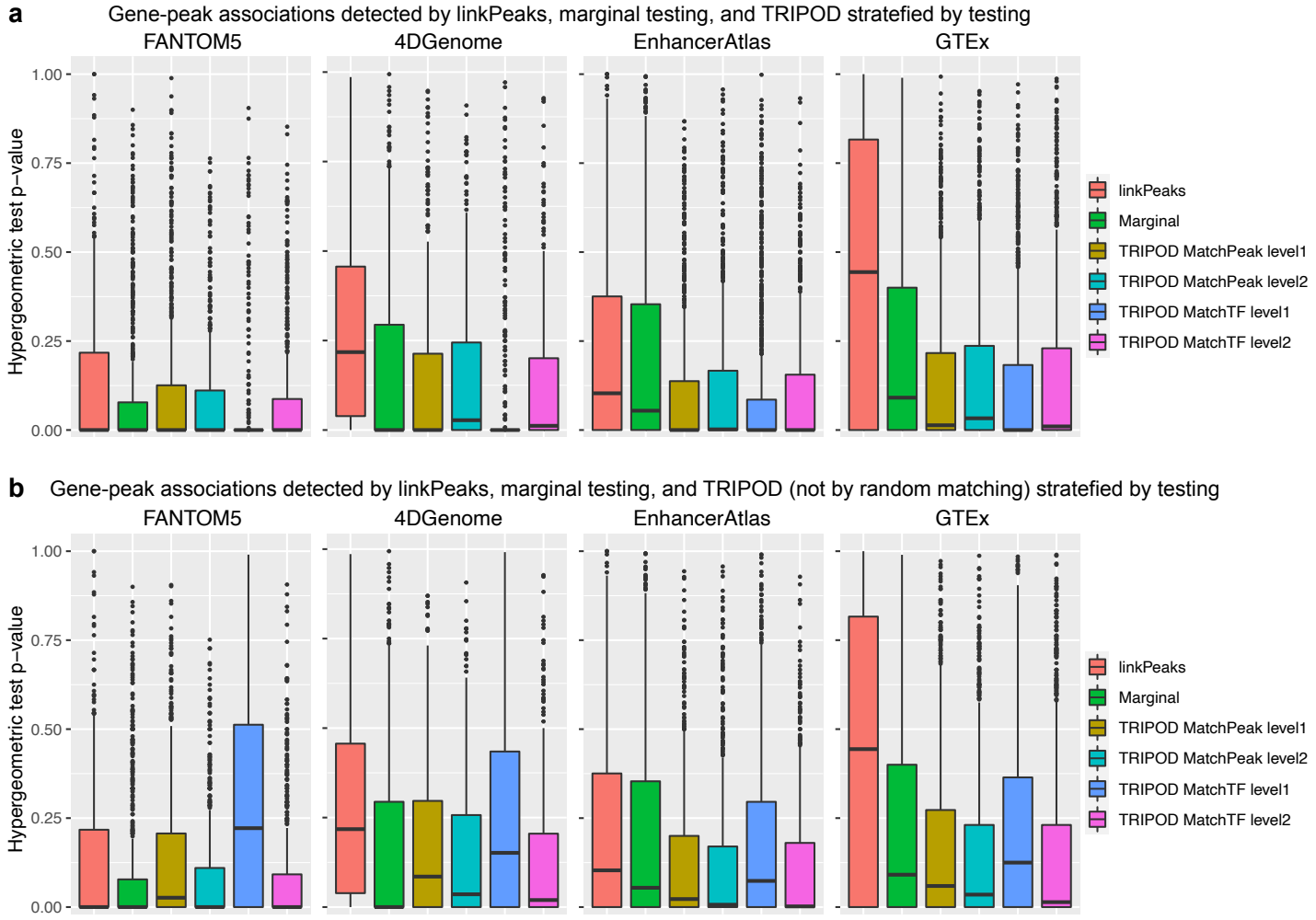

Fig. S14. Precision and recall rates of TF-gene validation by hTFtarget with different significance levels. Varying significance threshold alpha is adopted, in addition to the results shown in Fig. 4d. Related to Fig. 4.

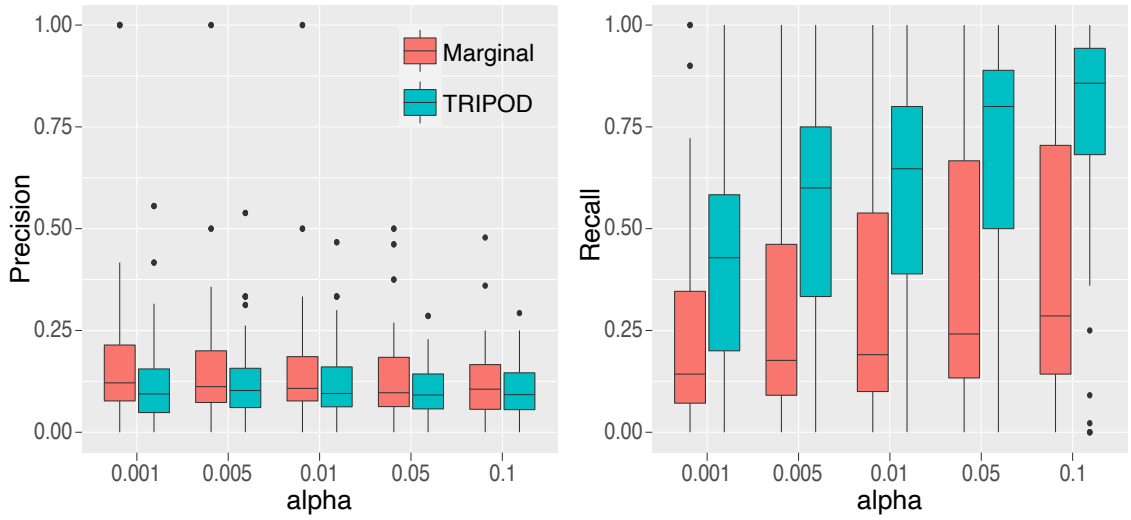

Fig. S15. Trio regulatory relationships identified by LinkPeaks, marginal association, and TRIPOD, and validation thereof using PLAC-seq data. a, Bar plots of the numbers of significant regulatory links detected by TRIPOD and marginal associations (FDR < 0.01). The numbers of peak-gene pairs and TF-gene pairs were obtained by collapsing trios by TFs and peaks, respectively. **b**, Heatmap showing the degree of enrichment of ATAC peaks in enhancer-promoter contacts by PLAC-seq (Zhu et al., 2019). **c**, Venn diagrams of the number of peak-gene pairs captured by PLAC-seq, marginal association between gene expression and peak accessibility, and various models as indicated on the top of each diagram. Related to Fig. 5.

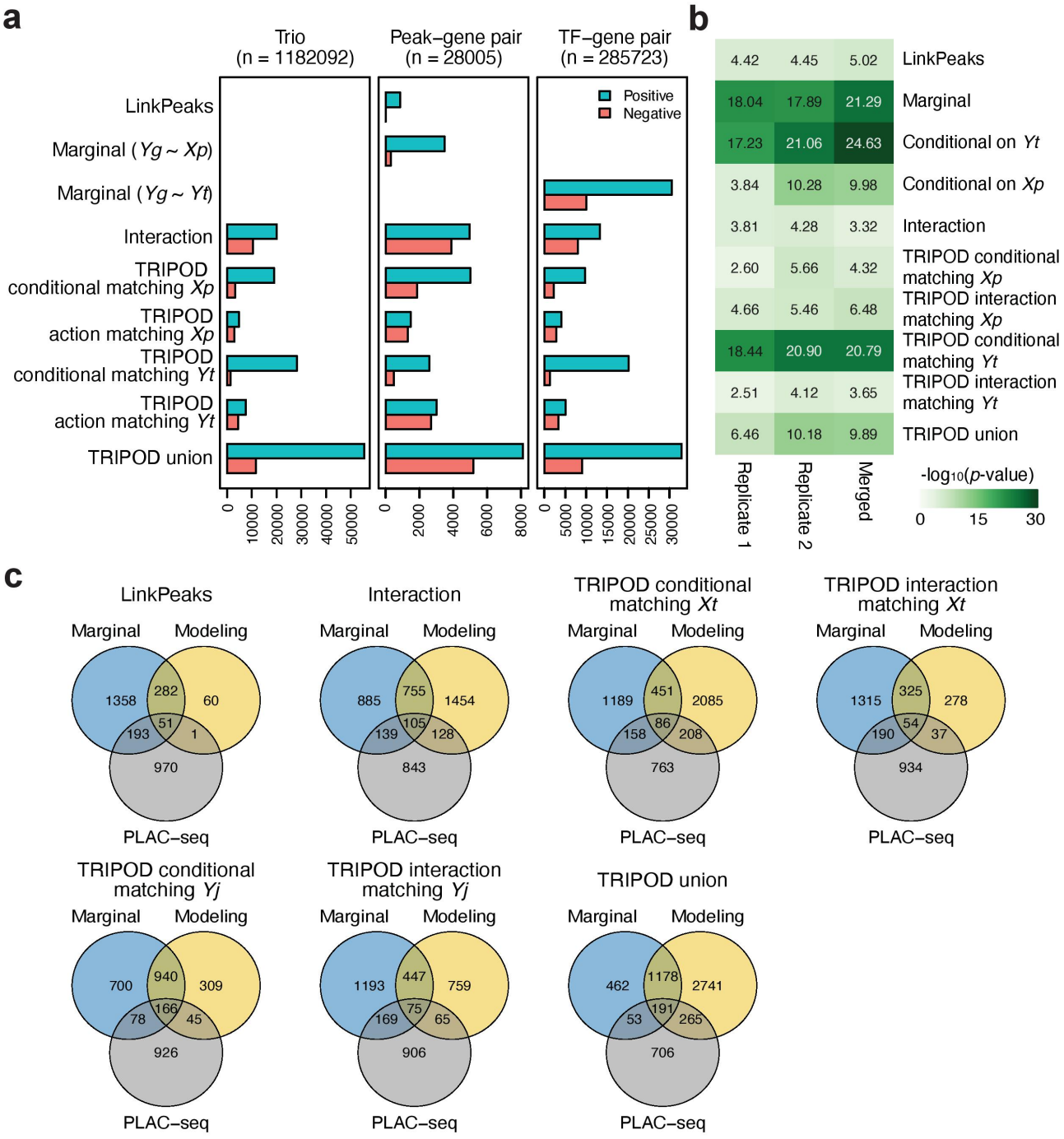

Fig. S16. Effects of window sizes on the model performance. a, Heatmap showing the degree of enrichment of ATAC peaks in enhancer-promoter contacts by PLAC-seq (Zhu et al., 2019) with window sizes corresponding to 50, 100, and 200 kb up and downstream from TSS. **b**, Peak-TF validation by ChIP-seq data for Olig2, Nuerog2, Eomes, and Tbr1 (Table 1) at window sizes of 50 kb (**b**), 100 kb (**c**), and 200 kb (**d**). Note that Olig2 ChIP-seq data from mature oligodendrocytes (mOL) serves as a negative control. Related to Fig. 5.

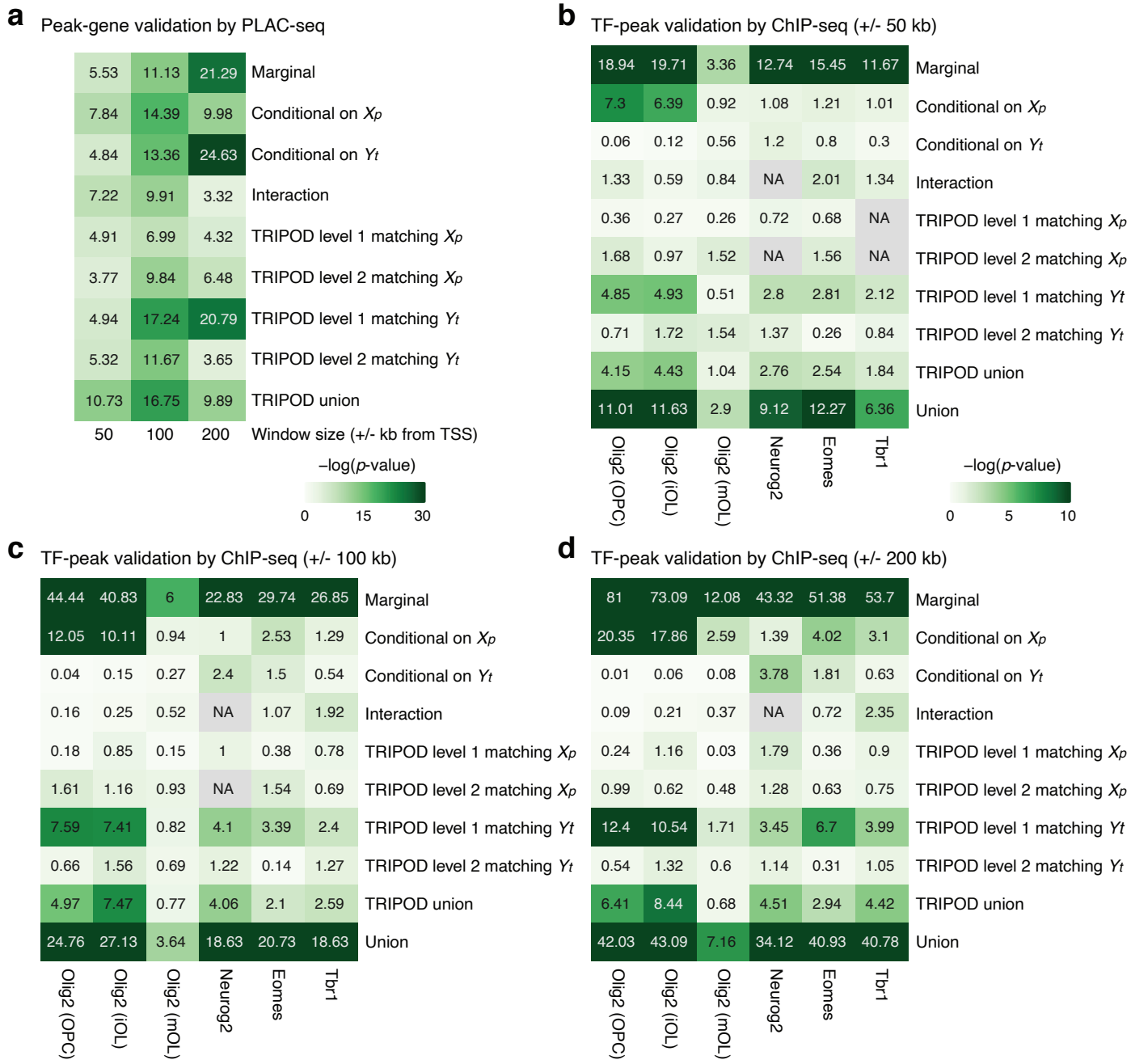

Fig. S17. Effects of cell-aggregate resolutions on the model performance. a, Heatmap showing the degree of enrichment of ATAC peaks in enhancer-promoter contacts by PLAC-seq (Zhu et al., 2019) with cell aggregates obtained at various clustering resolutions. The window size was set to 200 kb up and downstream of TSS. **b-d**, Peak-TF validation by ChIP-seq data (Table 1) for Olig2, Nuerog2, Eomes, and Tbr1 at clustering resolutions of 10 (**b**), 15 (**c**), and 20 (**d**) with the window size of 200 kb. Note that Olig2 ChIP-seq data from mature oligodendrocytes (mOL) serves as a negative control. Related to Fig. 5.

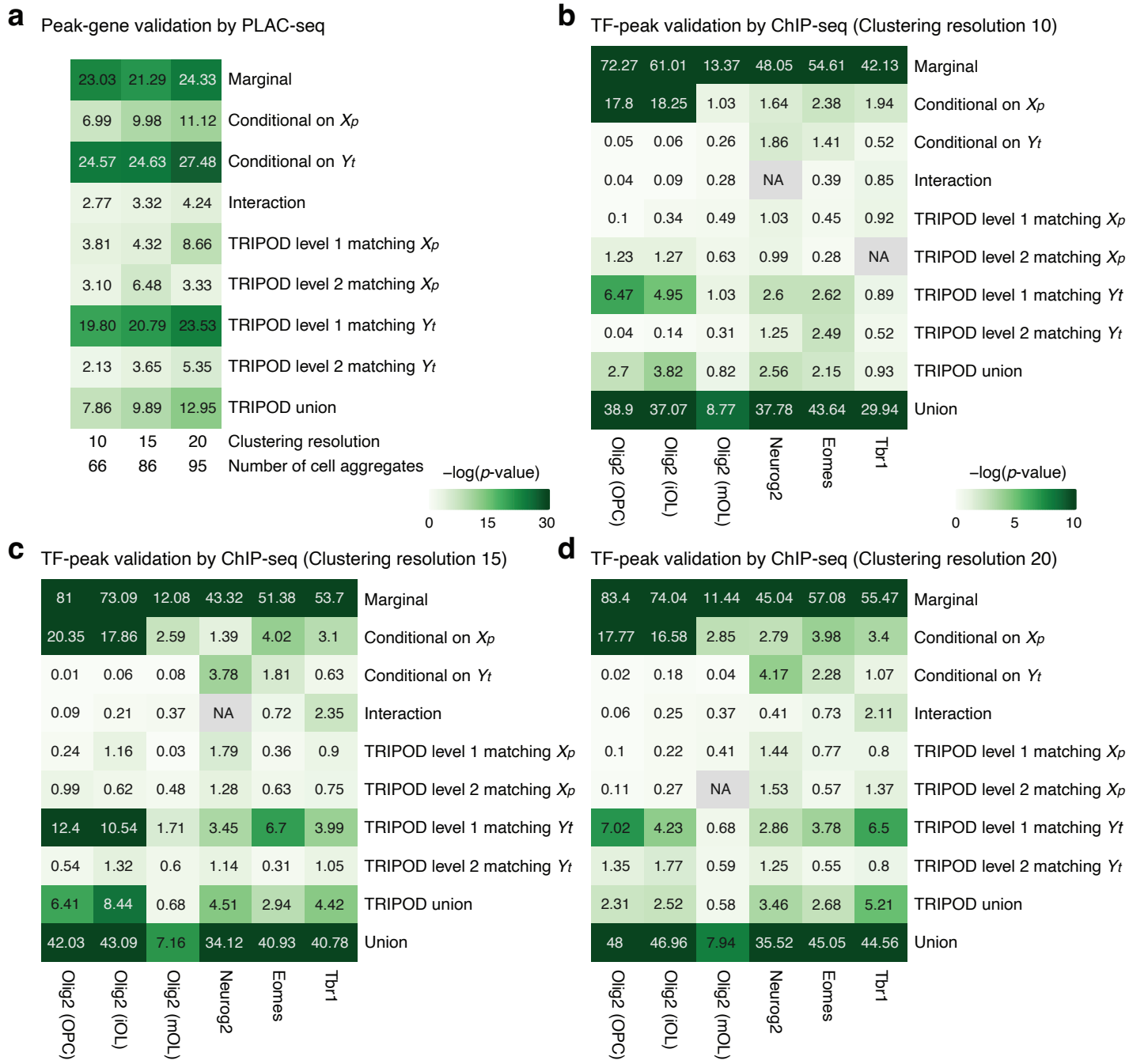

Fig. S18. Regulatory relationships between neurogenesis and gliogenesis pathways. The heatmap in the top panel show *p*-values for the marginal associations between TF and gene expression for 11 regulatory relationships indicated in the bottom. Note that the coefficient estimates were positive (i.e., greater than zero) for all cases. The bottom panel shows numbers of trio regulatory relationships with significantly positive coefficients (FDR < 0.01). Related to Fig. 5.

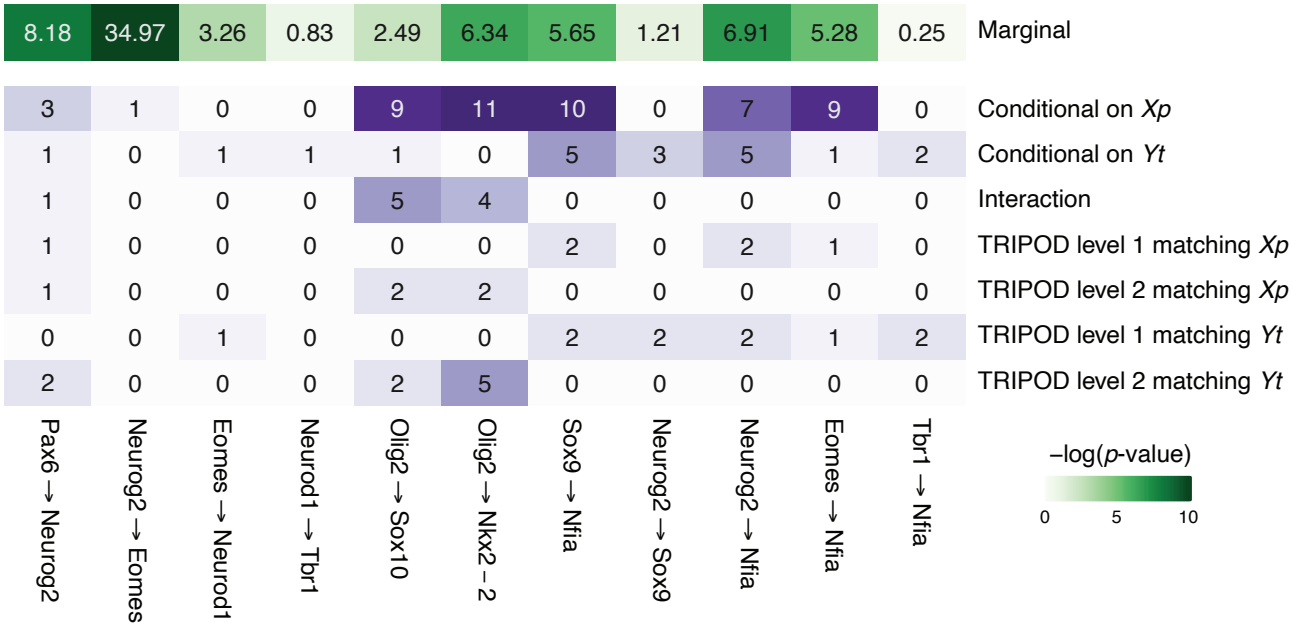

Fig. S19. Visualization of regulatory links representing possible crosstalks between neurogenesis- and gliogenesis-specific TF cascades. a, Putative regulation of *Nfia* by Neurog2, Eomes, and Tbr1. **b**, Putative regulation of *Sox9* by Neurog2. ChIP-seq peaks for the indicated TFs are included; arcs represent significant regulatory links inferred by TRIPOD. Related to Fig. 5.

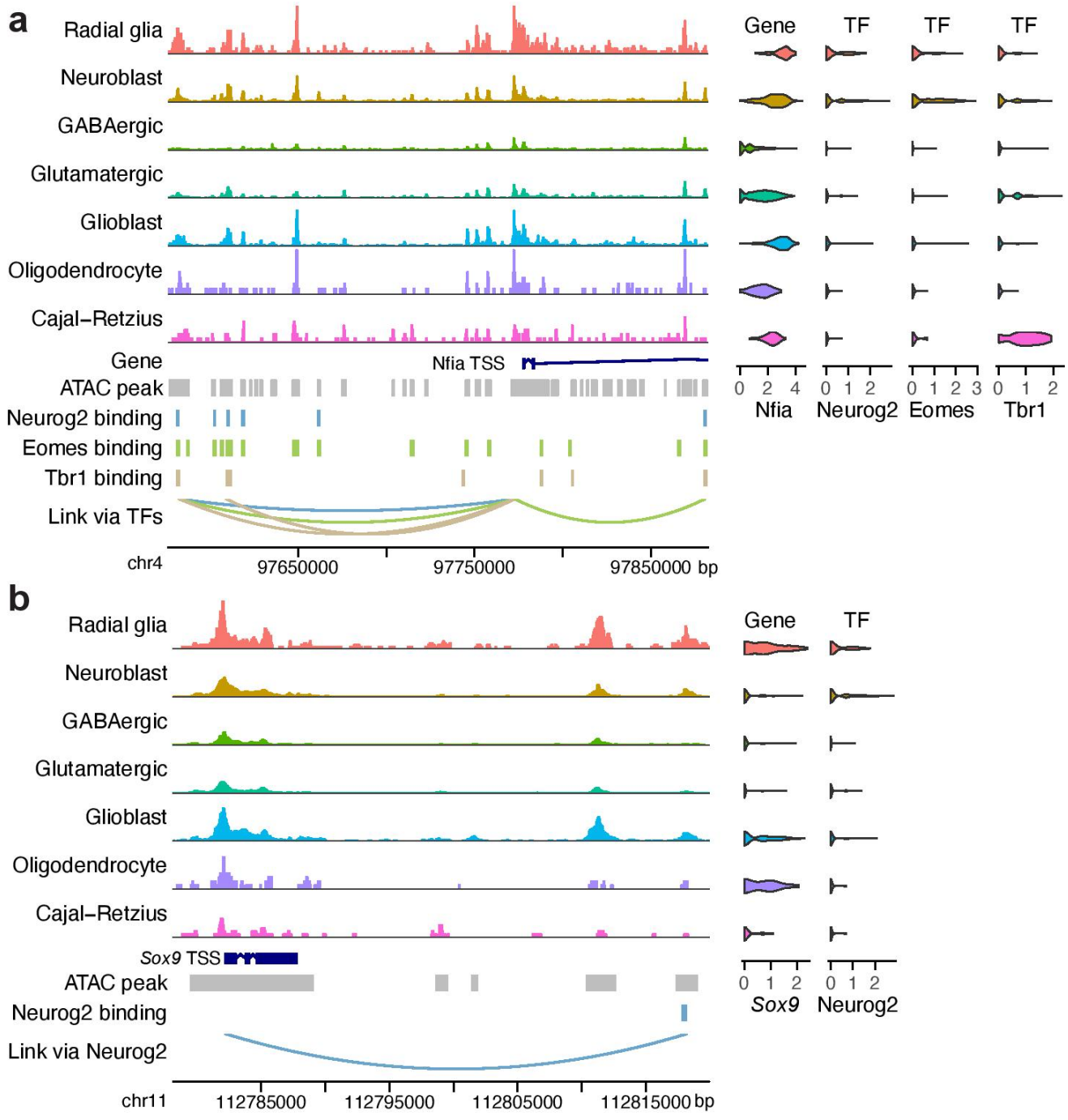

Fig. S20. Identification of putative cell-type- and cell-state-specific regulation in mouse embryonic brain. a-h, Visualization of eight example trios from the neurogenesis and gliogenesis TF cascades. The scatter plots (left) show TRIPOD's modeling fitting; the points represent cell aggregate and are colored based on cell types. The middle panels show cell-type-specific p-values from the sampling-based influence analyses. The colors on the UMAP embedding (right) correspond to the smoothed p-values from the sampling-based influence analyses along the differentiation trajectory. Genomic coordinates for the peaks are from mm10. Related to Fig. 5.

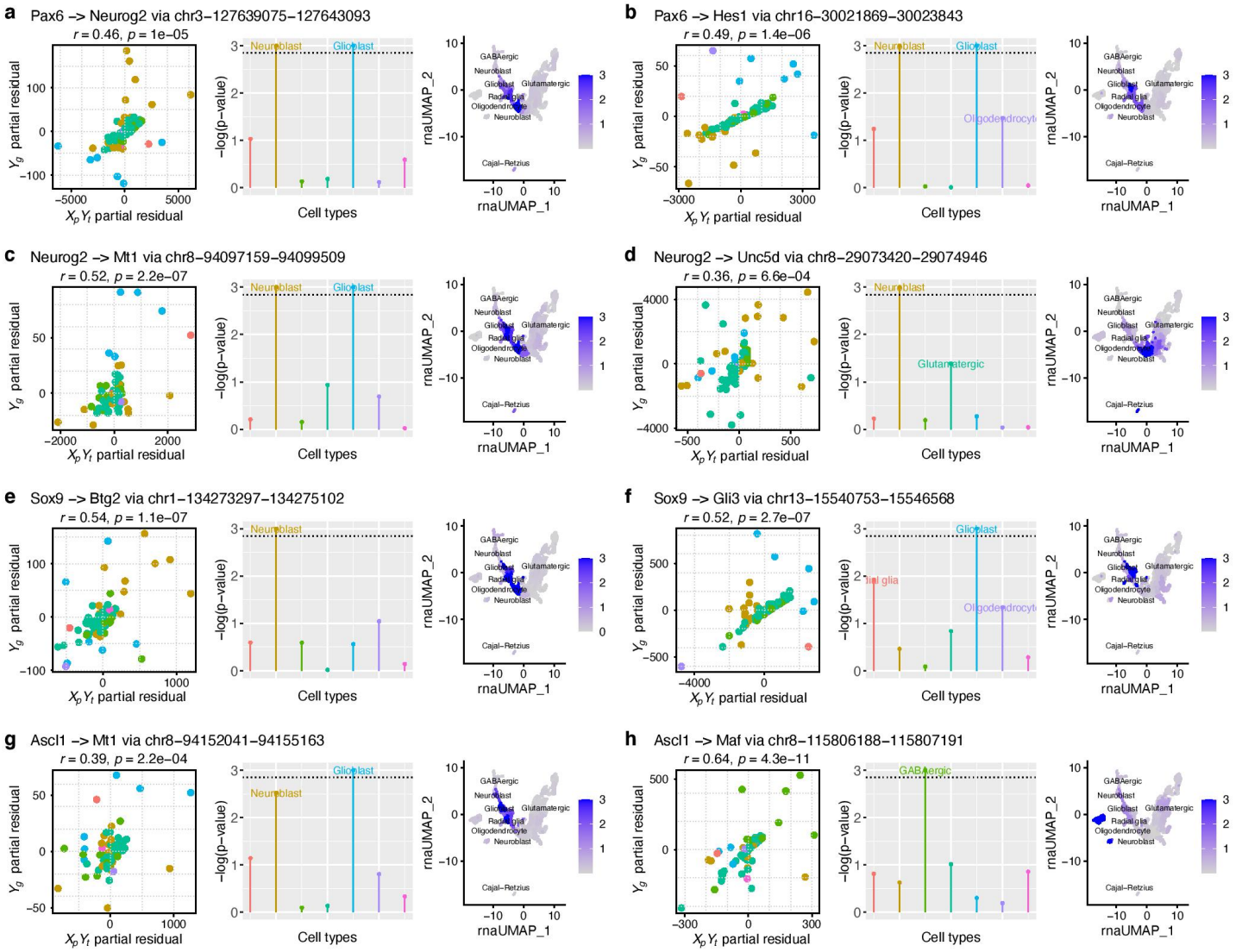

Fig. S21. Using TF RNA expression as a surrogate for protein expression. Tissue-specific RNA expression from RNA-seq and protein expression based on immunohistochemisty using tissue micro arrays are downloaded from the Human Protein Atlas (Uhlen et al., 2015). RNA expression levels are normalized as TPM; protein expression levels are categorial (i.e., not detected, low, medium, and high). a, Representative TFs from Fig. 3d with measured RNA and protein expression levels. b, All TFs with measured RNA and protein expression levels. While it is hard to measure protein expressions on the single-cell level, TF RNA expression from single-cell multiome serves as a good surrogate for protein expression. Related to STAR Methods.

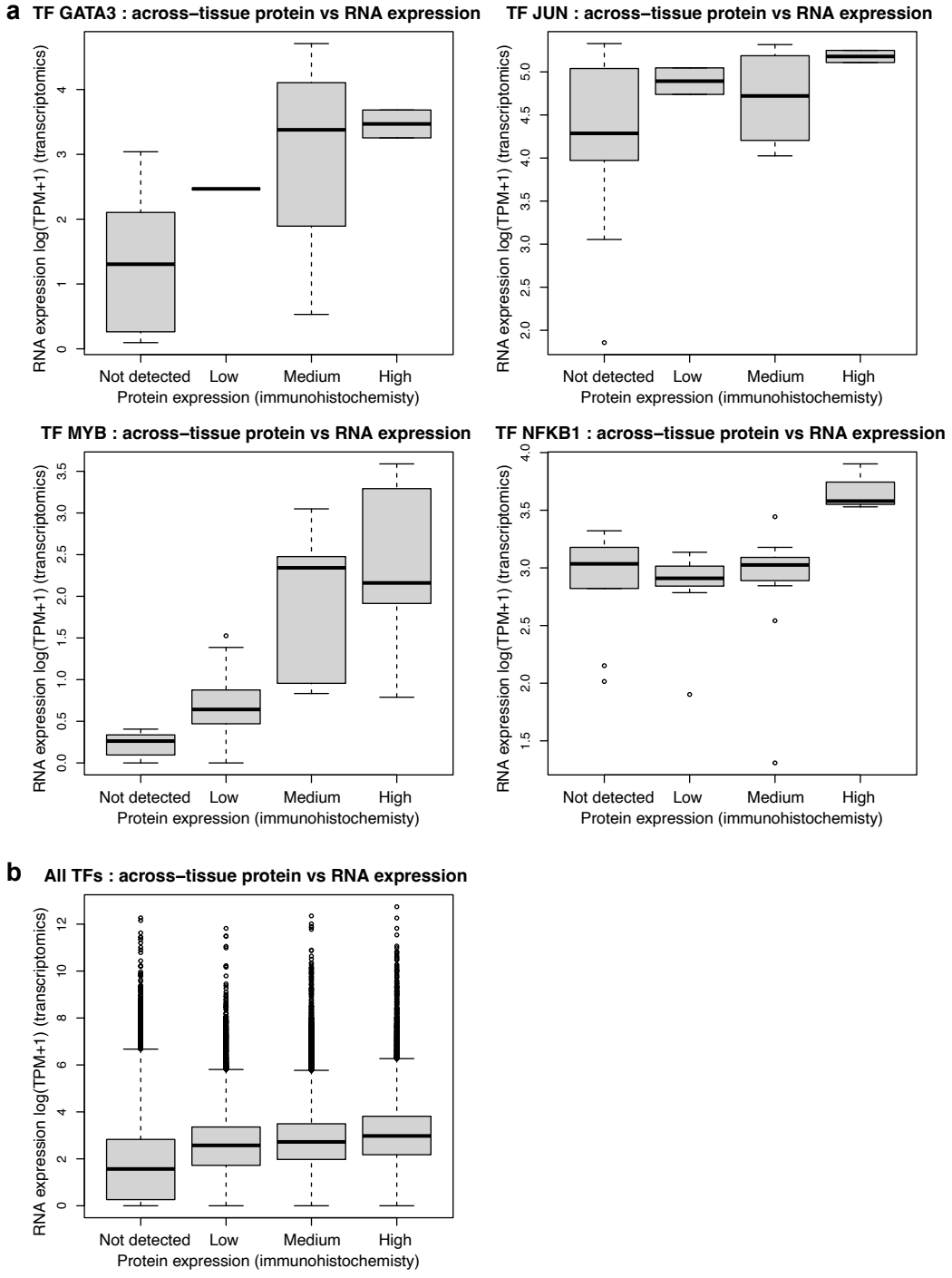

Fig. S22. Combining accessibilities of ATAC peaks containing the TF binding sites within the window centered at the gene's TSS does not improve EPIC's performance. In this analysis, we considered pairs of a TF and a target gene, and the pair was called positive if the model fitting yielded a positive coefficient estimate with FDR-adjusted p-value less than 0.01. To evaluate the model performance, we used sets of TF-gene pairs obtained from ChIP-seq of Olig2, Neurog2, Eomes, and Tbr1 (Table 1) as ground truths. Specifically, a true regulatory relationship was assumed if there existed at least one ChIP-seq peak within 200 kb up and downstream of the TSS of the target gene. The resultant receiver operator curves (ROCs) are in red. For comparison, ROCs for the models where individual peak regions were analyzed separately are also shown in blue. In this case, lists of significant regulatory trios (FDR < 0.01) were collapsed to obtain lists of TF-gene pairs. Related to STAR Methods.

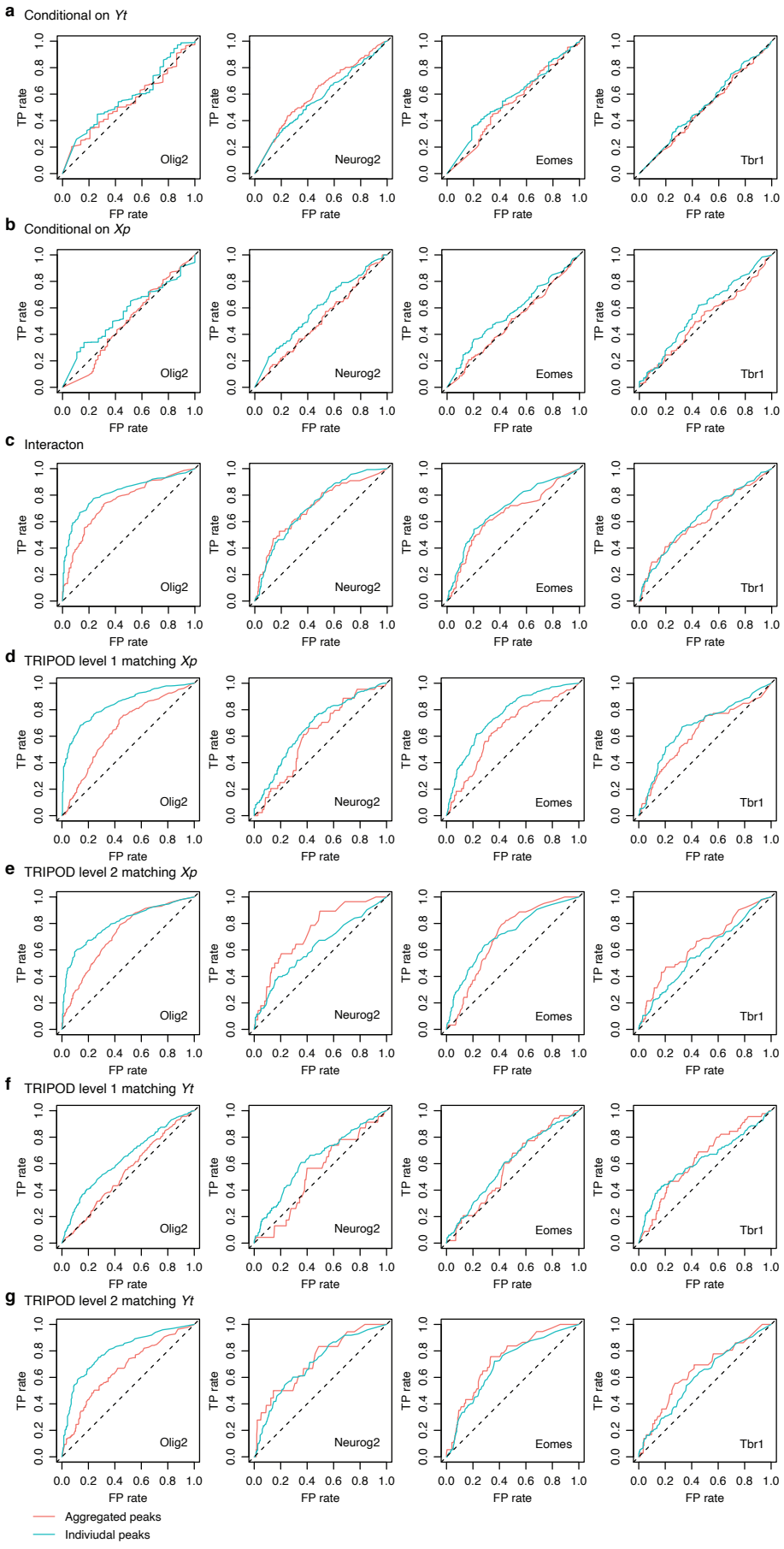
a Conditional on Yt
b Conditional on Xp
c Interacton
d TRIPOD level 1 matching Xp
e TRIPOD level 2 matching Xp
f TRIPOD level 1 matching Yt
g TRIPOD level 2 matching Yt
Olig2
Neurog2
Eomes
Tbr1
TP rate
FP rate
0.0 0.2 0.4 0.6 0.8 1.0
Aggregated peaks
Indiviudal peaks

Fig. S23. Assessing linear models for detecting conditional associations. Scatter plots comparing fittings from linear models and TRIPOD's level 1 and level 2 testing for example trios in **a**, PBMC and **b**, mouse skin. Genomic coordinates for the peaks are from hg38 for human and mm10 for mouse. Related to STAR Methods.

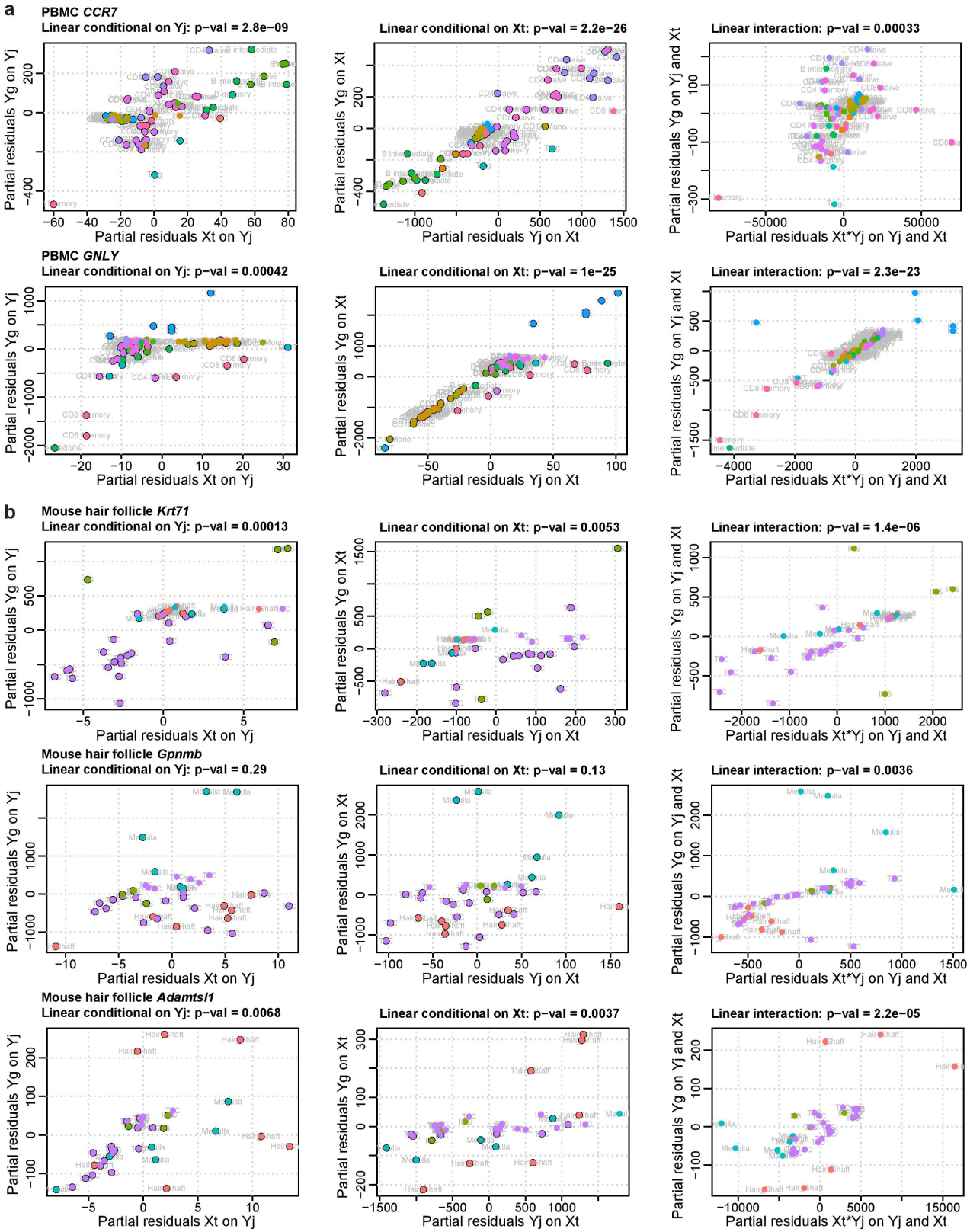

Fig. S24. Comparison of estimated coefficients from linear model and TRIPOD'S nonparametric model. a-d, Pairwise scatter plots comparing transformed coefficients from linear model and TRIPOD's nonparametric model for representative target genes, *CCR7*, *GNLY*, *FCGR3A*, and *MS4A1* from the PBMC data. γ denotes the coefficient for the interaction between TF expression and peak accessibility; α and β denote the coefficients for the partial gene-peak and gene-TF correlations, respectively. **e**, Same as a-d but across all genes. The three coefficients are fit using the linear model and TRIPOD's level 1 and level 2 testing, and their estimates are correlated on the global scale. However, the actual call sets are different, and the underlying models and assumptions are different. Related to STAR Methods.

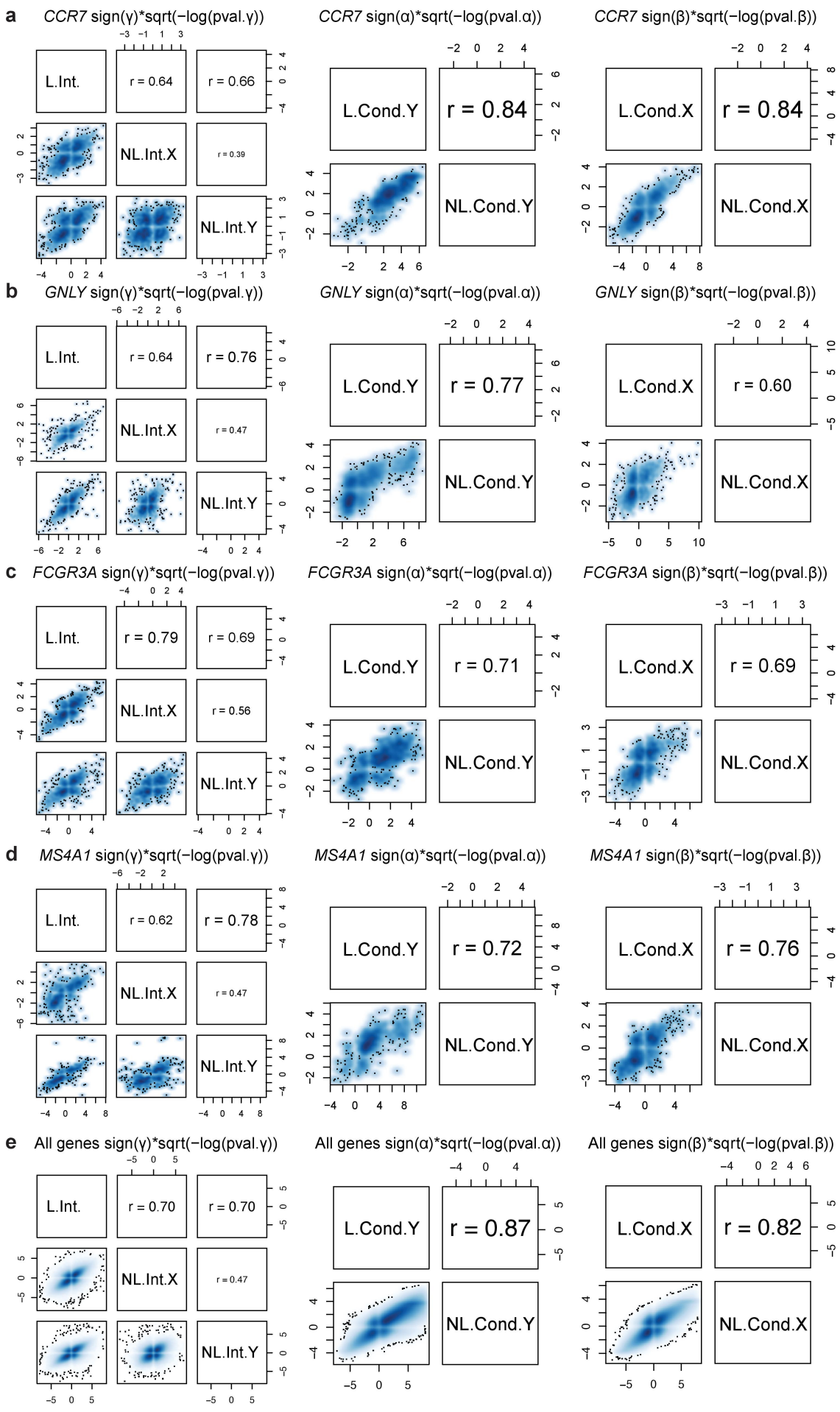
a
CCR7 sign(γ)*sqrt(−log(pval.γ))
CCR7 sign(α)*sqrt(−log(pval.α))
CCR7 sign(β)*sqrt(−log(pval.β))
L.Int.
r = 0.64
r = 0.66
NL.Int.X
r = 0.39
NL.Int.Y
L.Cond.Y
r = 0.84
NL.Cond.Y
L.Cond.X
r = 0.84
NL.Cond.X
b
GNLY sign(γ)*sqrt(−log(pval.γ))
GNLY sign(α)*sqrt(−log(pval.α))
GNLY sign(β)*sqrt(−log(pval.β))
L.Int.
r = 0.64
r = 0.76
NL.Int.X
r = 0.47
NL.Int.Y
L.Cond.Y
r = 0.77
NL.Cond.Y
L.Cond.X
r = 0.60
NL.Cond.X
c
FCGR3A sign(γ)*sqrt(−log(pval.γ))
FCGR3A sign(α)*sqrt(−log(pval.α))
FCGR3A sign(β)*sqrt(−log(pval.β))
L.Int.
r = 0.79
r = 0.69
NL.Int.X
r = 0.56
NL.Int.Y
L.Cond.Y
r = 0.71
NL.Cond.Y
L.Cond.X
r = 0.69
NL.Cond.X
d
MS4A1 sign(γ)*sqrt(−log(pval.γ))
MS4A1 sign(α)*sqrt(−log(pval.α))
MS4A1 sign(β)*sqrt(−log(pval.β))
L.Int.
r = 0.62
r = 0.78
NL.Int.X
r = 0.47
NL.Int.Y
L.Cond.Y
r = 0.72
NL.Cond.Y
L.Cond.X
r = 0.76
NL.Cond.X
e
All genes sign(γ)*sqrt(−log(pval.γ))
All genes sign(α)*sqrt(−log(pval.α))
All genes sign(β)*sqrt(−log(pval.β))
L.Int.
r = 0.70
r = 0.70
NL.Int.X
r = 0.47
NL.Int.Y
L.Cond.Y
r = 0.87
NL.Cond.Y
L.Cond.X
r = 0.82
NL.Cond.X

Fig. S25. Comparison of the trio regulatory relationships identified by linear model and TRIPOD's nonparametric model. a-d, Venn diagrams of the number of significant trios detected by linear and TRIPOD models for representative target genes, *CCR7*, *GNLY*, *FCGR3A*, and *MS4A1*. The left, middle, and right panels contain results from the interaction models, the models conditional on TF expression Y_t, and the models conditional on peak accessibility X_p. L.int., TRIPOD.Int.Y, TRIPOD.Int.X, L.Cond.Y, TRIPOD.Cond.Y, L.Cond.X, and TRIPOD.Cond.X represent linear interaction model, nonparametric interaction model matching by TF expression (TRIPOD level 2 test), nonparametric interaction model matching by peak accessibility (TRIPOD level 2 test), linear model conditional on TF expression, nonparametric conditional model matching by TF expression (TRIPOD level 1 test), linear model conditional on peak accessibility, and nonparametric conditional model matching by peak accessibility (TRIPOD level 1 test), respectively. Related to STAR Methods.

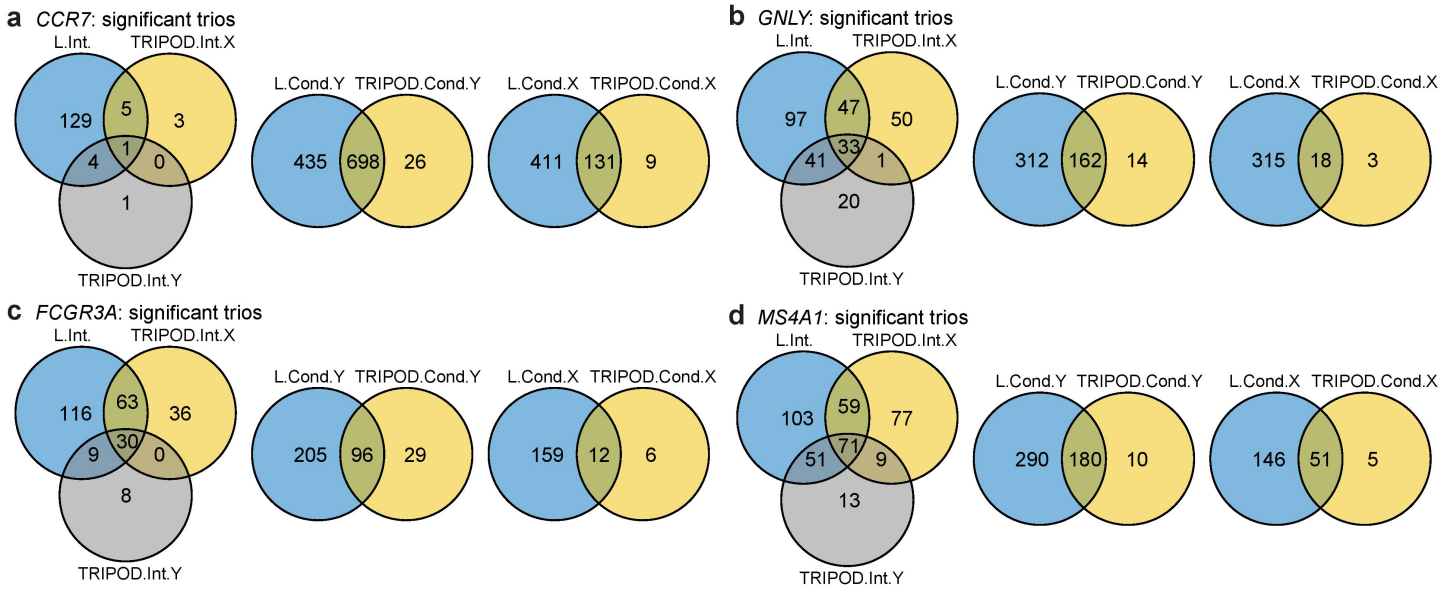

Supplementary Tables

Table S1. Single-cell RNA and ATAC multiomic datasets. Data adopted in this study from different tissues, organisms, and cell types using different protocols are summarized. The number of cells, peaks, and genes, as well as RNA read counts and ATAC read counts **a**, before and **b**, after quality control (QC) are summarized. Sources of data are also provided. Related to Fig. 1.

(A)

Organism	Tissue	Protocol	PMID or source	Before QC				
				Number of cells	Number of peaks	Number of genes	Mean cov. ATAC	Mean cov. RNA
Homo sapiens	PBMC	10X Genomics Multiome	10X Genomics	11909	108377	36601	20434	4402
Homo sapiens	PBMC	10X Genomics Multiome	10X Genomics	2714	156607	36601	20661	4344
Mus musculus	Embryonic brain at day 18	10X Genomics Multiome	10X Genomics	4881	139083	32285	20989	9486
Mus musculus	Skin late anagen	SHARE-seq	33098772	34774	344592	23296	4231	1259
Mus musculus	Adult brain cerebral cortex	SNARE-seq	31611697	10309	244544	33160	2656	1549
Mus musculus	Adult brain cerebral cortex	PAIRED-seq	31695190	15191	2614863	29624	1600	459

(B)

Organism	Tissue	Protocol	PMID or source	After QC				
				Number of cells	Number of peaks	Number of genes	Mean cov. ATAC	Mean cov. RNA
Homo sapiens	PBMC	10X Genomics Multiome	10X Genomics	7790	103755	14508	9611	3352
Homo sapiens	PBMC	10X Genomics Multiome	10X Genomics	2206	106056	36601	13534	4425
Mus musculus	Embryonic brain at day 18	10X Genomics Multiome	10X Genomics	3962	139083	14476	12520	8293
Mus musculus	Skin late anagen	SHARE-seq	33098772	29308	343783	15086	17886	1080
Mus musculus	Adult brain cerebral cortex	SNARE-seq	31611697	7533	244544	15332	12534	2053
Mus musculus	Adult brain cerebral cortex	PAIRED-seq	31695190	11292	118337	17858	3014	387

Table S2. Precision, recall, and joint F1 score with varying significance levels for TF-gene validation by knockTF. Varying significance level alpha is adopted, in addition to the fixed alpha shown in Fig. 4c. TRIPOD outperforms methods based on marginal association testing. Related to Fig. 4.

TF (knockTF)	alpha	Precision		Recall		F1 score	
		Marginal	TRIPOD	Marginal	TRIPOD	Marginal	TRIPOD
GATA3	0.001	0.0059	0.0108	0.0024	0.0049	0.0035	0.0067
	0.005	0.0051	0.0099	0.0024	0.0073	0.0033	0.0084
	0.01	0.005	0.0111	0.0024	0.0098	0.0033	0.0104
	0.05	0.0086	0.0097	0.0049	0.0122	0.0062	0.0108
JUN	0.001	0.1256	0.1445	0.0351	0.0437	0.0549	0.0671
	0.005	0.1244	0.123	0.0366	0.0487	0.0565	0.0698
	0.01	0.1238	0.1156	0.0373	0.0495	0.0573	0.0693
	0.05	0.1219	0.116	0.0387	0.0609	0.0588	0.0799
MAF	0.001	0	0.0917	0	0.0267	0	0.0414
	0.005	0	0.0906	0	0.0352	0	0.0507
	0.01	0	0.0871	0	0.0377	0	0.0526
	0.05	0.0071	0.0774	0.0012	0.0437	0.0021	0.0559
MYB	0.001	0	0.1468	0	0.0424	0	0.0658
	0.005	0.037	0.1324	0.0027	0.0716	0.005	0.0929
	0.01	0.0256	0.1265	0.0027	0.0849	0.0048	0.1016
	0.05	0.0282	0.1275	0.0053	0.1353	0.0089	0.1313
NFATC3	0.001	0.0403	0.0824	0.0047	0.0339	0.0084	0.0481
	0.005	0.0357	0.0835	0.0057	0.0452	0.0098	0.0587
	0.01	0.0291	0.0821	0.0057	0.049	0.0095	0.0614
	0.05	0.0247	0.0786	0.0066	0.0594	0.0104	0.0676
NFKB1	0.001	0	0.0076	0	0.0105	0	0.0088
	0.005	0	0.006	0	0.0105	0	0.0076
	0.01	0	0.0072	0	0.014	0	0.0095
	0.05	0	0.0087	0	0.021	0	0.0123
ZNF148	0.001	0	0.0013	0	0.027	0	0.0025
	0.005	0	0.0035	0	0.0811	0	0.0068
	0.01	0	0.0034	0	0.0811	0	0.0065
	0.05	0	0.003	0	0.0811	0	0.0058

Table S3. ChIP-seq data of human blood (B lymphocyte, T lymphocyte, and monocyte). Non-cancerous and cell-type-specific ChIP-seq data of human blood were downloaded from the Cistrome (Mei et al., 2017) portal to validate the peak-TF links in the PBMC single-cell multiomic data. PCR bottleneck coefficient (PBC) is used to estimate the rate of read duplication through PCR amplification; a good PBC score is ≥ 80%. PeaksFoldChangeAbove10 contains the number of peaks called by MACS2 (Zhang et al., 2008) with a fold change above 10. FRiP is used for evaluating the signal-to-noise ratio; a good FRiP score is ≥ 1%. PeaksUnionDHSRatio is the percentage of the merged top 5000 peaks (ordered by MACS2 q-value) that overlap with union DHS regions; this is expected to be ≥ 70%. Related to Table 1.

DCid	Species	GSMID	Factor	Cell_line	Cell_type	Tissue_type	FastQC	UniquelyMappedRatio	PBC	PeaksFoldChangeAbove10	FRiP	PeaksUnionDHSRatio
40022	Homo sapiens	GSM1121094	BRD4	None	B Lymphocyte	Blood	38	0.8193	0.955	1615	0.1565535	0.9436
40053	Homo sapiens	GSM1121098	CDK7	None	B Lymphocyte	Blood	38	0.7267	0.962	1230	0.05939275	0.9608
40226	Homo sapiens	GSM1195559	CDK9	None	B Lymphocyte	Blood	38	0.7745	0.937	4517	0.09261	0.9696
45178	Homo sapiens	GSM1003474	CTCF	None	B Lymphocyte	Blood	38	0.7908	0.904	27265	0.305596	0.9758
45179	Homo sapiens	GSM1003476	H2AZ	None	B Lymphocyte	Blood	37	0.7298	0.94	2524	0.1956965	0.975
40215	Homo sapiens	GSM1195560	IRF4	None	B Lymphocyte	Blood	38	0.8383	0.948	8535	0.13387325	0.9422
40216	Homo sapiens	GSM1195557	MED1	None	B Lymphocyte	Blood	38	0.5248	0.844	4058	0.14310625	0.9664
40233	Homo sapiens	GSM1195555	MED1	None	B Lymphocyte	Blood	38	0.6613	0.911	9273	0.2180545	0.954
40234	Homo sapiens	GSM1195556	MED1	None	B Lymphocyte	Blood	38	0.8217	0.963	4479	0.1278495	0.9472
5967	Homo sapiens	GSM762709	MYC	None	B Lymphocyte	Blood	29	0.7391	0.988	1211	0.048873002	0.9576
33439	Homo sapiens	GSM971344	POLR2A	None	B Lymphocyte	Blood	30	0.7135	0.922	4948	0.1402875	0.9746
33434	Homo sapiens	GSM971343	SMARCA4	None	B Lymphocyte	Blood	30	0.6431	0.909	2353	0.0451365	0.964
45444	Homo sapiens	GSM1003508	CTCF	None	Monocyte	Blood	37	0.7086	0.948	23384	0.243658	0.9718
45441	Homo sapiens	GSM1003548	H2AZ	None	Monocyte	Blood	37	0.8274	0.898	1674	0.11932275	0.975
41301	Homo sapiens	GSM1057025	IRF1	None	Monocyte	Blood	38	0.8155	0.932	11224	0.07846625	0.9264
41302	Homo sapiens	GSM1057026	IRF1	None	Monocyte	Blood	38	0.8212	0.943	3018	0.028401	0.945
41303	Homo sapiens	GSM1057027	IRF1	None	Monocyte	Blood	38	0.8198	0.877	5920	0.04798775	0.9316
81223	Homo sapiens	GSM2687534	RUNX1	None	Monocyte	Blood	38	0.7012	0.919	9496	0.31398225	0.9418
85986	Homo sapiens	GSM2804465	SPI1	None	Monocyte	Blood	39	0.7064	0.944	1283	0.038436584	0.9426
41287	Homo sapiens	GSM1057011	STAT1	None	Monocyte	Blood	39	0.8088	0.993	6006	0.11584575	0.976
41288	Homo sapiens	GSM1057012	STAT1	None	Monocyte	Blood	39	0.7591	0.995	1501	0.0587395	0.9728
41289	Homo sapiens	GSM1057013	STAT1	None	Monocyte	Blood	39	0.8118	0.993	11395	0.15686975	0.9774
82662	Homo sapiens	GSM2679938	T	None	Monocyte	Blood	39	0.8392	0.992	11428	0.14325775	0.9586
81224	Homo sapiens	GSM2687535	TET2	None	Monocyte	Blood	38	0.6452	0.79	2851	0.22890725	0.7862
36301	Homo sapiens	GSM823379	BRD4	None	T Lymphocyte	Blood	39	0.6184	0.803	1025	0.02953575	0.9652
38389	Homo sapiens	GSM1022944	BRD4	None	T Lymphocyte	Blood	38	0.7591	0.968	1092	0.04322775	0.9644
3060	Homo sapiens	GSM325895	CTCF	None	T Lymphocyte	Blood	29	0.5214	0.902	15633	0.253560996	0.9716
44090	Homo sapiens	GSM1056928	ETS1	None	T Lymphocyte	Blood	37	0.5843	0.965	1319	0.0132305	0.96
44092	Homo sapiens	GSM1056930	ETS1	None	T Lymphocyte	Blood	39	0.803	0.909	3052	0.0402015	0.9594
44093	Homo sapiens	GSM1056931	ETS1	None	T Lymphocyte	Blood	38	0.7048	0.905	1559	0.02145925	0.956
44094	Homo sapiens	GSM1056932	ETS1	None	T Lymphocyte	Blood	39	0.7582	0.903	2587	0.039202	0.9608
4459	Homo sapiens	GSM393968	POLR2A	None	T Lymphocyte	Blood	27	0.5922	0.982	3068	0.04810575	0.972
36302	Homo sapiens	GSM823380	POLR2A	None	T Lymphocyte	Blood	39	0.7371	0.8	10180	0.2364385	0.9728
38342	Homo sapiens	GSM1022949	POLR2A	None	T Lymphocyte	Blood	39	0.736	0.968	5581	0.08956125	0.973
38361	Homo sapiens	GSM1022946	POLR2A	None	T Lymphocyte	Blood	38	0.7341	0.964	6984	0.1400275	0.975
38431	Homo sapiens	GSM1022950	POLR2A	None	T Lymphocyte	Blood	39	0.7477	0.97	6222	0.09659675	0.971
38433	Homo sapiens	GSM1022948	POLR2A	None	T Lymphocyte	Blood	39	0.7713	0.974	1407	0.03362775	0.9644
38454	Homo sapiens	GSM1022945	POLR2A	None	T Lymphocyte	Blood	39	0.7491	0.957	5196	0.079669	0.9732
47435	Homo sapiens	GSM1201946	REST	None	T Lymphocyte	Blood	37	0.6073	0.886	1840	0.0628475	0.916
44097	Homo sapiens	GSM1056935	RUNX1	None	T Lymphocyte	Blood	39	0.7136	0.886	1187	0.0181065	0.9504
53629	Homo sapiens	GSM1577746	STAT5B	None	T Lymphocyte	Blood	37	0.7536	0.767	8377	0.1459865	0.95
53630	Homo sapiens	GSM1577747	STAT5B	None	T Lymphocyte	Blood	37	0.7297	0.708	8462	0.1848495	0.9604
53631	Homo sapiens	GSM1577748	STAT5B	None	T Lymphocyte	Blood	38	0.6881	0.676	2727	0.07564975	0.804
5195	Homo sapiens	GSM630810	YY1	None	T Lymphocyte	Blood	20	0.5189	0.783	3788	0.119051698	0.9708